

Shadow, Hawking radiation, and thermodynamics of Letelier black hole in electromagnetic universe with Barrow entropy

İzzet Sakallı¹, Erdem Sucu¹², Ahmad Al-Badawi²³, Faizuddin Ahmed³⁴

¹*Physics Department, Eastern Mediterranean University, Famagusta, 99628 North Cyprus, via Mersin 10, Türkiye*

²*Department of Physics, Al-Hussein Bin Talal University, 71111, Ma'an, Jordan*

³*Department of Physics, The Assam Royal Global University, Guwahati, 781035, Assam, India*

Abstract

We present a theoretical investigation of a static, spherically symmetric Letelier black hole immersed in an electromagnetic universe, characterized by the cloud of strings parameter α and the electromagnetic universe parameter a . The spacetime structure is established by deriving the event horizon radii, curvature invariants, and isometric embedding diagrams that visualize the horizon expansion with increasing string density. The Hawking temperature and Bekenstein-Hawking entropy are computed, revealing monotonic suppression of thermal emission as α increases. The photon sphere and shadow radius are obtained analytically, demonstrating that both parameters enlarge the apparent black hole silhouette compared to the Schwarzschild geometry. We extend the shadow analysis to homogeneous and inhomogeneous plasma environments, quantifying the frequency-dependent reductions in observed shadow size. The optical appearance is decomposed into direct emission, lensed emission, and photon ring contributions following Event Horizon Telescope methodology. The Hawking radiation spectra and energy emission rates are computed for scalar, electromagnetic, and Dirac fields, with greybody factors calculated using the rigorous bounds method. The thermodynamic phase structure is analyzed within the Barrow entropy framework, where the heat capacity exhibits second-order phase transitions and the Joule-Thomson expansion reveals cooling-heating inversion curves governed by the model parameters. The stability under fermionic perturbations is established through supersymmetric quantum mechanics, confirming that the positive chirality effective potential remains strictly positive outside the horizon across the parameter space. Our results provide theoretical predictions testable by current shadow observations and future gravitational wave measurements.

Keywords: Letelier black hole; Cloud of strings; Black hole shadow; Hawking radiation; Barrow entropy

Contents

1	Introduction	3
2	Spacetime Structure and Horizon Properties of the Letelier BH in EMU	4
2.1	Metric Structure and Parameter Space	4
2.2	EH Structure and Existence Conditions	5
2.3	Lapse Function Behavior	5
2.4	Asymptotic Structure and Curvature Invariants	5
2.5	Isometric Embedding Diagrams	5
2.6	Surface Gravity and Thermodynamic Quantities	6
3	PS, Shadow, and Optical Appearance	7
3.1	PS and Effective Potential	8
3.2	Vacuum Shadow	9
3.3	Optical Appearance and Emission Decomposition	9
3.4	Shadow Images: Parameter Space Exploration	10
3.5	Shadow in Homogeneous Plasma	11
3.6	Shadow in Inhomogeneous Plasma	13
3.7	Photon Trajectories	13
3.8	Observational Implications and EHT Constraints	13

¹izzet.sakalli@emu.edu.tr; ORCID: 0000-0001-7827-9476

²erdemsc07@gmail.com; ORCID: 0009-0000-3619-1492

³ahmadbadawi@ahu.edu.jo; ORCID: 0000-0002-7633-3048

⁴faizuddinahmed15@gmail.com; ORCID: 0000-0003-2196-9622

4	HR and Energy Emission	14
4.1	Hawking Temperature	14
4.2	Total Emission Power	15
4.3	HR Spectra for Different Spin Fields	15
5	Phase Structure and JTE with Barrow Entropy	16
5.1	Heat Capacity and Thermodynamic Stability	18
5.2	JTE	18
6	Dirac Field Perturbations	20
6.1	Dirac Equation in Curved Spacetime	20
6.2	Effective Potential Analysis	20
6.3	Greybody Factors for Dirac Fields	21
6.4	Stability Under Dirac Perturbations	21
7	Conclusions	22

1 Introduction

The study of BHs has occupied a central position in gravitational physics since the pioneering work of Schwarzschild, who obtained the first exact solution to Einstein’s field equations describing the exterior geometry of a spherically symmetric, static mass distribution [1]. Over the past century, BH physics has evolved from a theoretical curiosity into an active area of observational astronomy, driven by the detection of gravitational waves (GWs) from binary BH mergers by the LIGO-Virgo-KAGRA collaboration [2, 3] and the imaging of supermassive BH shadows by the Event Horizon Telescope (EHT) [4, 5]. These groundbreaking observations have opened new windows for testing general relativity (GR) in the strong-field regime and searching for deviations that might signal the presence of new physics beyond the standard paradigm [6, 7].

Among the various extensions of the Schwarzschild geometry, BH solutions embedded in matter fields and topological defect configurations have attracted considerable attention. Letelier introduced a class of spacetimes describing BHs surrounded by a CoS, which represents a collection of one-dimensional topological defects formed during symmetry-breaking phase transitions in the early universe [8]. The CoS generates an anisotropic energy-momentum tensor with the distinctive equation of state $p_r = -\rho$, where the radial pressure equals the negative of the energy density [9, 10]. This configuration produces a deficit solid angle at spatial infinity, modifying the asymptotic structure of the spacetime in a manner analogous to global monopoles and cosmic strings [11–16]. The Letelier solution has been extensively studied in the context of thermodynamics [17], quasinormal modes (QNMs) [18], gravitational lensing [19], and particle dynamics [20], revealing that the CoS parameter introduces measurable deviations from the standard Schwarzschild predictions.

Parallel developments in cosmology have established the importance of electromagnetic (EM) backgrounds and quintessence fields in modeling the accelerated expansion of the universe [21, 22]. The EMU model, originally proposed by Bonnor and later extended by various authors, describes spacetimes permeated by a background EM field that modifies the effective gravitational potential experienced by test particles [23, 24]. When a BH is immersed in such an EMU, the metric function acquires additional terms that mimic the behavior of a Reissner-Nordström (RN) geometry with an effective charge parameter determined by the EM background strength [25]. The combination of CoS and EMU effects produces a two-parameter family of BH solutions that interpolates continuously between the Schwarzschild, RN, and pure Letelier spacetimes, offering a rich phenomenology for studying how multiple modifications interact in strong gravitational fields [26–32].

The thermodynamic properties of BHs have been a subject of intense investigation since Bekenstein and Hawking established the foundations of BH thermodynamics in the 1970s [33, 34]. The discovery that BHs radiate

thermally with a temperature proportional to the surface gravity opened profound connections between gravity, quantum mechanics, and statistical physics [35]. Recent developments have extended the thermodynamic description to include modified entropy formulations, among which the Barrow entropy has emerged as a particularly interesting proposal [36]. Barrow suggested that quantum-gravitational effects may deform the event horizon (EH) geometry, leading to an effectively fractal surface characterized by a deformation parameter $\Delta \in [0, 1]$ [37]. This modification has been applied to cosmological settings [38–40] and BH thermodynamics [41], revealing novel phase transition structures and modified thermodynamic relations that could encode signatures of quantum gravity.

The optical appearance of BHs, particularly the shadow cast by the photon sphere (PS) against a luminous background, has become a primary observable for testing gravity theories [42, 43]. The EHT observations of M87* and Sgr A* have provided shadow size measurements with approximately 10% precision, enabling constraints on deviations from the Kerr geometry [44, 45]. The shadow radius depends sensitively on the near-horizon geometry and the properties of null geodesics, making it a powerful probe of BH parameters and potential modifications to GR [46]. Plasma effects in the accretion environment can further modify the apparent shadow size through frequency-dependent refraction, requiring careful modeling of both the spacetime geometry and the surrounding medium [47–54]. Moreover, the Hawking radiation (HR) spectrum and greybody factors provide additional channels for probing BH physics. The greybody factors quantify the transmission probability of HR through the effective potential barrier surrounding the BH and depend on the spin of the emitted particles [55, 56]. For fermionic fields, the Dirac equation in curved spacetime leads to a pair of supersymmetric (SUSY) partner potentials whose structure determines both the emission characteristics and the dynamical stability of the BH under perturbations [57, 58]. The stability analysis is particularly important for establishing whether a given BH solution represents a physically viable configuration that can exist in nature without spontaneous decay [59].

Motivated by these developments, we investigate in this paper the Letelier BH immersed in an EMU, examining its geometric, thermodynamic, optical, and radiative properties. Our aims are threefold. First, we seek to establish the complete spacetime structure, including the EH configuration, curvature invariants, and asymptotic behavior, for the two-parameter family of solutions characterized by the CoS parameter α and the EMU parameter a . Second, we aim to compute the observable signatures relevant for current and future BH observations, including the shadow radius, photon ring (PR) structure, and HR spectra for different spin fields. Third, we explore the thermodynamic phase structure within the Barrow entropy framework, analyzing the heat capacity and Joule-Thomson expansion (JTE) to identify phase tran-

sitions and cooling-heating regimes. The combination of CoS and EMU effects produces distinctive phenomenology that distinguishes this solution from both the standard Schwarzschild geometry and its individual modifications. The CoS parameter α enters the metric function as a constant shift, reducing the asymptotic value of the lapse function and producing a deficit angle geometry at spatial infinity. The EMU parameter a introduces an effective charge-like term that scales as $1/r^2$, mimicking the RN behavior while arising from the background EM field rather than an intrinsic BH charge. The interplay between these two effects modifies the EH structure, PS location, Hawking temperature, and effective potentials for field perturbations in ways that can be disentangled through careful parameter studies.

Our analysis employs a combination of analytical derivations and numerical computations. The EH radii and thermodynamic quantities are obtained in closed form, allowing direct comparison with known limiting cases. The shadow radius and greybody factors are computed using established techniques, including the Visser bounds method for transmission coefficients. The Barrow entropy framework is applied to study the heat capacity and JTE coefficient, revealing connections between the phase transition structure and inversion curves. The stability under Dirac perturbations is established using the SUSY quantum mechanics formalism, exploiting the factorized structure of the effective potentials. From an observational perspective, the results presented in this work provide theoretical predictions that can be compared with EHT shadow measurements and future GW ringdown observations. The shadow radius varies by up to 48% across the parameter space examined, a deviation well within the sensitivity of current and next-generation instruments. The HR suppression caused by the CoS could explain the survival of primordial BHs in certain mass ranges, with implications for dark matter searches and the diffuse gamma-ray background. The modified phase structure within the Barrow entropy framework offers potential connections to quantum gravity phenomenology that could be tested through precision thermodynamic measurements [60, 61].

The paper is organized as follows. In Sec. 2, we establish the spacetime structure and horizon properties of the Letelier BH in EMU, deriving the metric function, EH radii, curvature invariants, and thermodynamic quantities including the Hawking temperature and entropy. Section 3 presents the optical properties, including the PS and shadow analysis in vacuum and plasma environments, the emission decomposition into direct, lensed, and PR contributions, and the photon trajectory structure. The HR properties and energy emission rates are computed in Sec. 4, where we analyze the spectra for scalar, EM, and Dirac fields and discuss the implications for BH evaporation. Section 5 explores the phase structure and JTE within the Barrow entropy framework, identifying second-order phase transitions and inversion curves. The Dirac field perturbations and stability analysis are presented in

Sec. 6, where we derive the effective potentials, compute greybody factors, and establish dynamical stability using the SUSY formalism. Finally, Sec. 7 summarizes our conclusions and outlines directions for future research.

2 Spacetime Structure and Horizon Properties of the Letelier BH in EMU

This section establishes the geometric foundation of the Letelier BH embedded in an EMU. We derive the EH structure, examine the behavior of the metric function across the parameter space, compute the curvature invariants, and visualize the spatial geometry through isometric embedding diagrams. The interplay between the CoS parameter α and the EMU parameter a produces a two-parameter family of BH solutions that interpolates continuously between the Schwarzschild, RN, and pure Letelier spacetimes.

2.1 Metric Structure and Parameter Space

We consider a static, spherically symmetric BH solution describing a Letelier spacetime surrounded by a CoS and immersed in an EMU. The line element takes the standard form [8, 17]

$$ds^2 = -f(r) dt^2 + \frac{dr^2}{f(r)} + r^2 (d\theta^2 + \sin^2 \theta d\phi^2), \quad (1)$$

where the lapse function $f(r)$ encapsulates all gravitational modifications [62]:

$$f(r) = 1 - \alpha - \frac{2M}{r} + \frac{M^2}{r^2} (1 - a^2). \quad (2)$$

Here M denotes the BH mass as measured by an asymptotic observer, $\alpha \in (0, 1)$ is the CoS parameter characterizing the energy density of the string cloud permeating the spacetime, and $a \in [0, 1]$ is the EMU parameter that quantifies the strength of the electromagnetic background. The CoS arises from a network of one-dimensional topological defects formed during symmetry-breaking phase transitions in the early universe [11, 63]. Such string configurations generate an anisotropic energy-momentum tensor with the distinctive equation of state $p_r = -\rho$, where the radial pressure equals the negative of the energy density [64, 65].

The metric function (2) encompasses several well-known spacetimes as special limits. Setting $\alpha = 0$ and $a = 1$ yields $f(r) = 1 - 2M/r$, recovering the standard Schwarzschild solution that describes an isolated, uncharged, non-rotating BH in vacuum [1]. For $a = 1$ with $\alpha \neq 0$, we obtain $f(r) = 1 - \alpha - 2M/r$, which describes the Letelier spacetime with a deficit solid angle $\delta\Omega = 4\pi\alpha$ due to the CoS [8]. This deficit angle removes a wedge from the solid angle at spatial infinity, producing a conical geometry analogous

to cosmic string spacetimes [11, 66]. Setting $\alpha = 0$ with $a \neq 1$ gives $f(r) = 1 - 2M/r + M^2(1 - a^2)/r^2$, representing a RN-like BH where the effective charge parameter is $Q_{\text{eff}}^2 = M^2(1 - a^2)$. The complete solution with both $\alpha \neq 0$ and $a \neq 1$ captures the combined effects of topological defects and electromagnetic backgrounds, offering a fertile ground to study how multiple modifications to the Schwarzschild geometry interact.

2.2 EH Structure and Existence Conditions

The EH radii are determined by the roots of $f(r_h) = 0$. Rearranging Eq. (2), we obtain the quadratic equation

$$(1 - \alpha)r_h^2 - 2Mr_h + M^2(1 - a^2) = 0. \quad (3)$$

Applying the quadratic formula yields the outer (r_+) and inner (r_-) horizon radii:

$$r_{\pm} = \frac{M \left(1 \pm \sqrt{1 - (1 - \alpha)(1 - a^2)} \right)}{1 - \alpha}. \quad (4)$$

For real-valued horizons, the discriminant must be non-negative, imposing the constraint $(1 - \alpha)(1 - a^2) \leq 1$. This condition is automatically satisfied throughout the allowed parameter range $\alpha \in (0, 1)$ and $a \in [0, 1]$, ensuring that the BH possesses at least one horizon. The equality defines the extremal limit where both horizons merge at $r_{\text{ext}} = M/(1 - \alpha)$, corresponding to a degenerate horizon with vanishing surface gravity [67].

In the pure Letelier limit ($a = 1$), the $1/r^2$ term vanishes, and the horizons simplify to $r_+ = 2M/(1 - \alpha)$ and $r_- = 0$. The outer horizon expands monotonically with increasing α , reaching $r_+ = 4M$ at $\alpha = 0.5$ and diverging as $\alpha \rightarrow 1$. In the pure EMU limit ($\alpha = 0$), we recover $r_{\pm} = M(1 \pm a)$, which matches the RN horizon structure upon identifying $Q_{\text{eff}} = M\sqrt{1 - a^2}$. The extremal configuration occurs at $a = 0$, where both horizons coalesce at $r_+ = r_- = M$.

Table 1 presents representative horizon radii for various combinations of α and a . The rows marked with \star correspond to the 3D embedding configurations displayed in Fig. 2. Several trends emerge from the tabulated values. As α increases at fixed a , the outer horizon r_+ expands monotonically, reflecting the gravitational dilution caused by the CoS. The inner horizon r_- decreases with increasing α , eventually disappearing in the single-horizon configurations at $a = 1$. For fixed α , increasing a from 0 to 1 causes the two horizons to separate, transitioning from the near-extremal regime to the single-horizon Letelier geometry.

2.3 Lapse Function Behavior

The behavior of the lapse function $f(r)$ determines the causal structure of the spacetime and the nature of particle orbits. Figure 1 illustrates $f(r)$ for various parameter

choices. Panel (a) shows the variation with the CoS parameter α at fixed $a = 0.5$. As α increases, two effects become apparent: the asymptotic value $f(\infty) = 1 - \alpha$ decreases, reflecting the deficit angle geometry, and the outer EH radius r_+ shifts outward. For $\alpha = 0.5$, the horizon is located at $r_+ \approx 3.6M$, nearly twice the Schwarzschild value. Panel (b) displays the variation with the EMU parameter a at fixed $\alpha = 0.1$. As a approaches unity, the RN-like $1/r^2$ term diminishes, recovering the single-horizon Letelier geometry. For small a , the metric function exhibits a local maximum between the two horizons, characteristic of the RN-type causal structure with a Cauchy horizon at r_- . Panel (c) presents special limiting cases including the Schwarzschild, pure Letelier, RN-like, and extremal configurations. The intersections with $f(r) = 0$ (dashed gray line) identify the horizon locations.

2.4 Asymptotic Structure and Curvature Invariants

At large distances, the metric function expands as

$$f(r) \approx (1 - \alpha) - \frac{2M}{r} + \mathcal{O}(r^{-2}), \quad (5)$$

indicating that the spacetime approaches a deficit angle geometry characterized by α rather than flat Minkowski space [12]. The solid angle at spatial infinity is reduced to $4\pi(1 - \alpha)$, producing a globally conical structure that distinguishes the Letelier BH from standard asymptotically flat solutions.

The curvature invariants quantify the gravitational field strength in a coordinate-independent manner. The Ricci scalar evaluates to

$$R = \frac{2\alpha}{r^2}, \quad (6)$$

which vanishes in the absence of the CoS ($\alpha = 0$) but diverges as $r \rightarrow 0$ for any non-zero α . The non-vanishing Ricci scalar reflects the energy-momentum contribution from the CoS, which acts as an anisotropic fluid with equation of state $p_r = -\rho$ [8, 68]. This equation of state characterizes Nambu-Goto strings and produces a traceless stress tensor in the string-orthogonal directions.

The Kretschmann scalar $K = R_{\mu\nu\rho\sigma}R^{\mu\nu\rho\sigma}$ takes the form

$$K = \frac{48M^2}{r^6} - \frac{96M^3(1 - a^2)}{r^7} + \frac{56M^4(1 - a^2)^2}{r^8}, \quad (7)$$

which diverges as $r \rightarrow 0$, confirming the presence of a curvature singularity at the origin [69]. The leading r^{-6} term matches the Schwarzschild contribution, while the subleading terms arise from the EMU modification. The Kretschmann scalar is independent of α , indicating that the CoS contributes only to the Ricci curvature and not to the Weyl tensor.

2.5 Isometric Embedding Diagrams

To visualize the spatial geometry outside the EH, we construct isometric embedding diagrams following the stan-

α	a	r_+/M	r_-/M	Configuration
0.00	0.0	1.0000	1.0000	Extremal BH
0.00	0.5	1.8660	0.1340	Non-extremal BH ★
0.00	1.0	2.0000	–	Schwarzschild BH ★
0.10	0.5	1.7445	0.4777	Non-extremal BH
0.10	1.0	2.2222	–	Letelier BH ★
0.20	0.5	2.0406	0.4594	Non-extremal BH ★
0.20	1.0	2.5000	–	Single horizon BH
0.30	0.5	2.4132	0.4440	Non-extremal BH
0.50	0.5	3.5811	0.4189	Non-extremal BH ★
0.50	1.0	4.0000	–	Single horizon BH ★
0.70	0.5	6.2678	0.3989	Non-extremal BH
0.90	1.0	20.0000	–	Single horizon BH

Table 1: Representative EH radii for the Letelier BH in EMU with $M = 1$. Rows marked with ★ correspond to the 3D embedding configurations in Fig. 2. The dash (–) indicates configurations with a single horizon where $r_- = 0$.

dard procedure [70]. For a constant-time ($t = \text{const}$), equatorial ($\theta = \pi/2$) slice, the induced 2D metric reads

$$d\sigma^2 = \frac{dr^2}{f(r)} + r^2 d\phi^2. \quad (8)$$

This metric can be embedded in 3D Euclidean space (r, ϕ, Z) provided the embedding height $Z(r)$ satisfies

$$\frac{dZ}{dr} = \sqrt{\frac{1}{f(r)} - 1}. \quad (9)$$

The embedding is valid for $f(r) < 1$, which holds outside the EH throughout the parameter space.

Figure 2 displays 3D embedding diagrams for six representative configurations. Panel (i) shows the Schwarzschild limit ($\alpha = 0, a = 1$) with the familiar funnel shape and horizon at $r_+ = 2M$. Panel (ii) presents the RN-like case ($\alpha = 0, a = 0.5$), where the effective charge term modifies the near-horizon geometry, producing a narrower throat. Panel (iii) illustrates the pure Letelier BH ($\alpha = 0.1, a = 1$) with an expanded horizon at $r_+ = 2.22M$. Panels (iv)–(vi) demonstrate the combined effects: as α increases, the EH expands dramatically, reaching $r_+ = 3.58M$ at ($\alpha = 0.5, a = 0.5$) and $r_+ = 4.00M$ at ($\alpha = 0.5, a = 1$). The red ring in each diagram marks the EH location r_+ , and the black spiral represents a timelike geodesic spiraling toward the singularity.

2.6 Surface Gravity and Thermodynamic Quantities

The surface gravity at the outer horizon governs the Hawking temperature and initiates the discussion of BH thermodynamics [71, 72, 72]. For the metric (1), the surface

$$\kappa = \frac{1}{2} \left| \frac{df}{dr} \right|_{r=r_+} = \frac{M}{r_+^2} \left| 1 - \frac{M(1-a^2)}{r_+} \right|. \quad (10)$$

Substituting the horizon radius from Eq. (4) and simplifying yields

$$\kappa = \frac{(1-\alpha)\sqrt{1-(1-\alpha)(1-a^2)}}{2M}. \quad (11)$$

In the Schwarzschild limit ($\alpha = 0, a = 1$), we recover $\kappa = 1/(4M)$.

The Hawking temperature follows from the Euclidean periodicity argument as $T_H = \kappa/(2\pi)$ [71, 73]:

$$T_H = \frac{(1-\alpha)\sqrt{1-(1-\alpha)(1-a^2)}}{4\pi M}, \quad (12)$$

which reduces to $T_H^{\text{Sch}} = 1/(8\pi M)$ in the Schwarzschild limit. The temperature decreases monotonically with increasing α , reaching zero in the extremal limit. This behavior has important consequences for HR and the BH evaporation timescale, as explored in Sec. 7.

The BH entropy follows from the Bekenstein-Hawking area law [72, 74]:

$$S = \frac{A}{4} = \pi r_+^2, \quad (13)$$

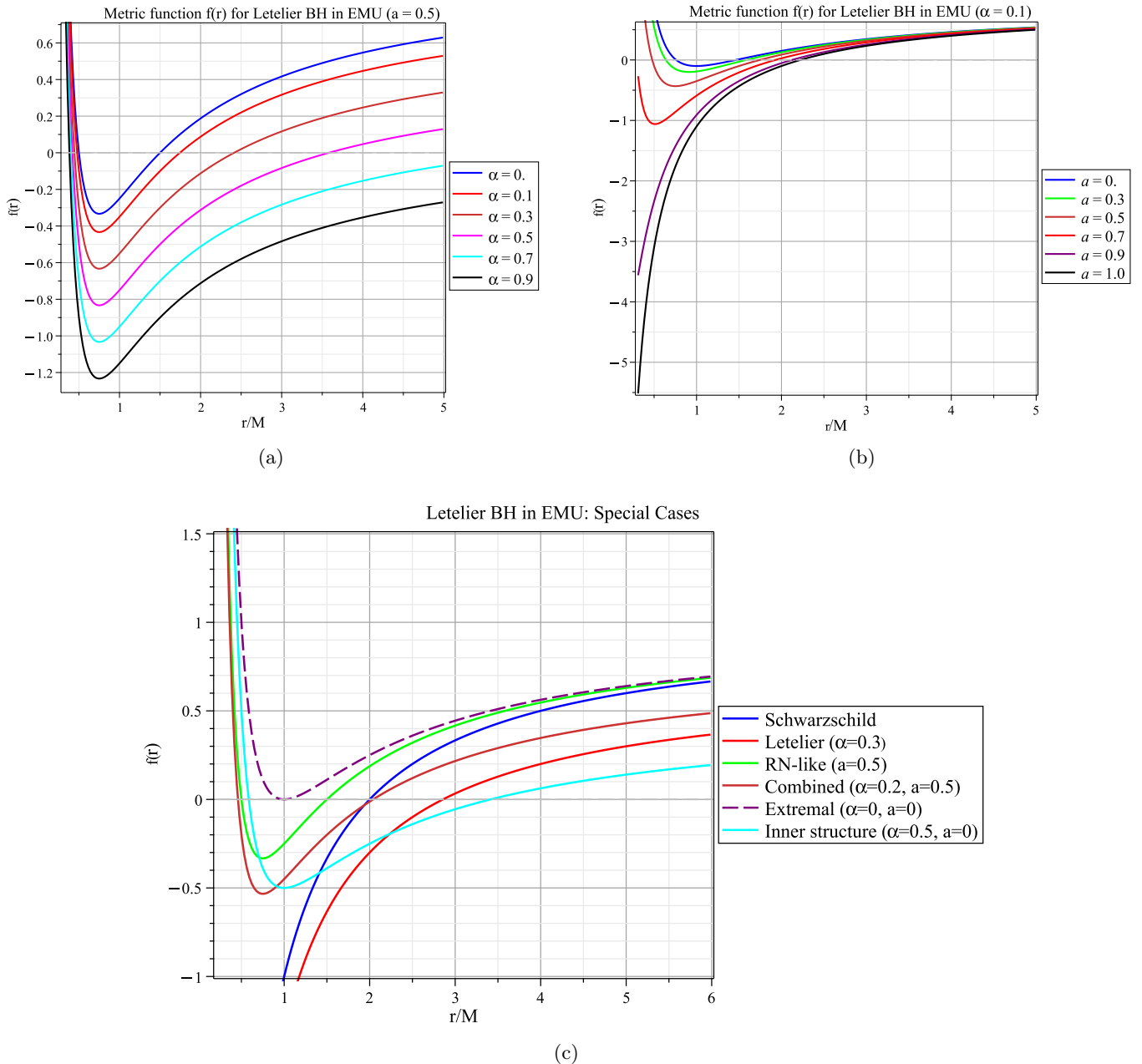
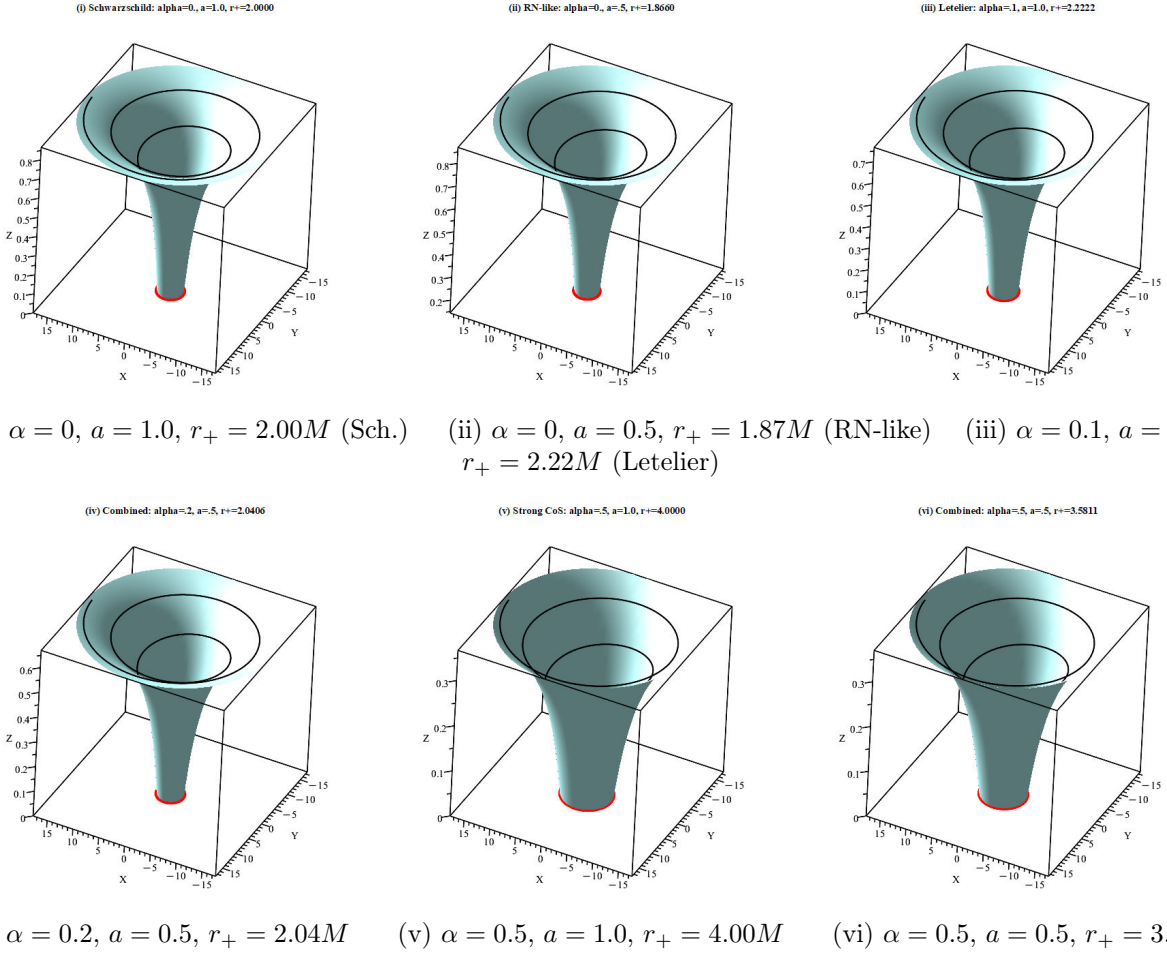


Figure 1: Lapse function $f(r)$ for the Letelier BH in EMU with $M = 1$. (a) Variation with CoS parameter $\alpha \in \{0.0, 0.1, 0.3, 0.5, 0.7, 0.9\}$ at fixed $a = 0.5$. (b) Variation with EMU parameter $a \in \{0.0, 0.3, 0.5, 0.7, 0.9, 1.0\}$ at fixed $\alpha = 0.1$. (c) Special limiting cases including Schwarzschild, Letelier, RN-like, and extremal configurations. The dashed gray line marks $f(r) = 0$, with intersections indicating horizon locations.

where $A = 4\pi r_+^2$ is the horizon area. Since r_+ increases with α , the entropy of the Letelier BH in EMU exceeds that of the Schwarzschild BH of equal mass, reflecting the expanded horizon area. The first law of BH thermodynamics extends to include variations of the CoS and EMU parameters: $dM = T_H dS + \Phi_\alpha d\alpha + \Phi_a da$, where Φ_α and Φ_a are the conjugate potentials associated with the string density and electromagnetic background [75].

3 PS, Shadow, and Optical Appearance

In this section, we analyze the optical properties of the Letelier BH in EMU. We begin by deriving the PS radius and shadow observables in vacuum, then extend the analysis to plasma environments. Subsequently, we investigate the optical appearance of the BH by decomposing the observed intensity into direct emission, lensed emission, and PR contributions. Finally, photon trajectories are examined to illustrate the light deflection behavior near the



(i) $\alpha = 0, a = 1.0, r_+ = 2.00M$ (Sch.) (ii) $\alpha = 0, a = 0.5, r_+ = 1.87M$ (RN-like) (iii) $\alpha = 0.1, a = 1.0, r_+ = 2.22M$ (Letelier)

Figure 2: 3D isometric embedding diagrams of the Letelier BH in EMU for six parameter configurations with $M = 1$. The turquoise surface represents the spatial geometry from the EH outward to $r = 15M$, the red ring marks the outer horizon r_+ , and the black curve depicts an infalling trajectory. The funnel widens as α increases, reflecting the EH expansion induced by the CoS.

BH.

$V'_{\text{eff}}(r_{ps}) = 0$ and $V''_{\text{eff}}(r_{ps}) < 0$ yield the PS radius [78]

3.1 PS and Effective Potential

The motion of photons around the Letelier BH in EMU is governed by the null geodesic equations. For photons confined to the equatorial plane ($\theta = \pi/2$), the effective potential takes the form [76, 77]

$$V_{\text{eff}} = \frac{L^2}{r^2} f(r) = \frac{L^2}{r^2} \left(1 - \alpha - \frac{2M}{r} + \frac{M^2(1 - a^2)}{r^2} \right), \quad (14)$$

where L is the conserved angular momentum of the photon. The effective potential encapsulates the combined gravitational influence of the BH mass, the CoS parameter α , and the EMU correction characterized by the parameter a .

The PS corresponds to unstable circular orbits located at the maximum of the effective potential. The conditions

$$r_{ps} = \frac{M \left(3 + \sqrt{9 - 8(1 - \alpha)(1 - a^2)} \right)}{2(1 - \alpha)}. \quad (15)$$

In the Schwarzschild limit ($\alpha = 0, a = 1$), we recover the standard result $r_{ps} = 3M$.

Figure 3 displays the effective potential for null geodesics under varying parameter conditions. In panel (a), we observe that increasing α at fixed $a = 0.5$ reduces the peak height and shifts the maximum outward. This behavior reflects the gravitational dilution caused by the CoS, which effectively reduces the gravitational binding and allows photons to orbit at larger radii. In panel (b), decreasing the EMU parameter a at fixed $\alpha = 0.1$ increases the peak height and shifts it inward. This indicates that stronger electromagnetic corrections enhance the effective gravitational confinement near the BH. The peak location in each case corresponds precisely to the PS radius r_{ps} .

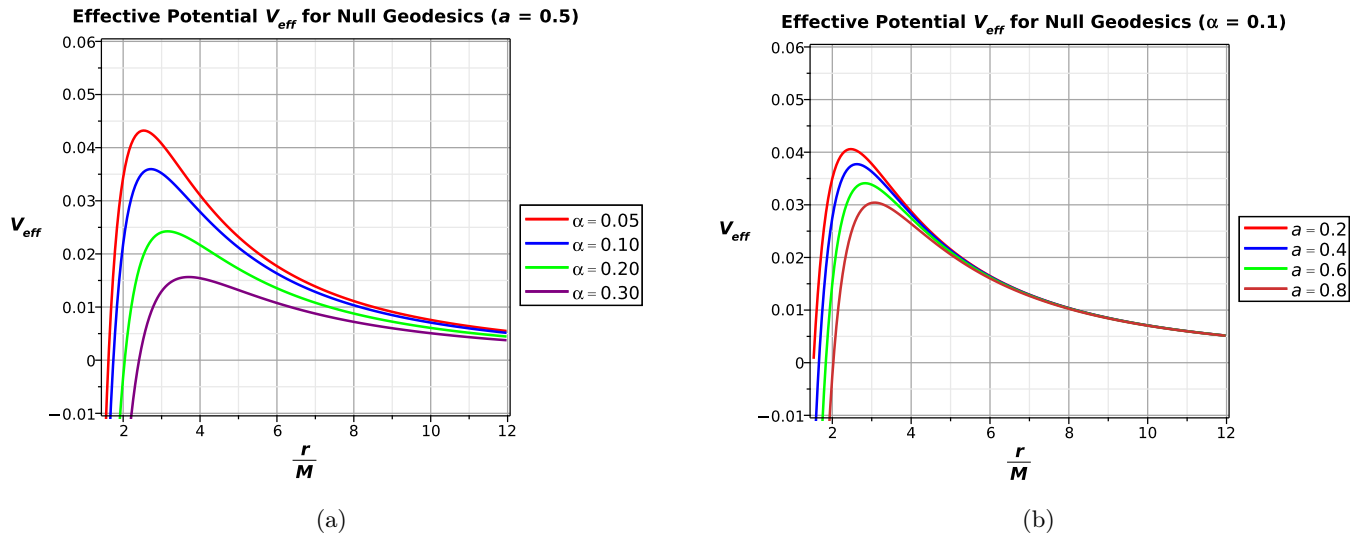


Figure 3: Effective potential V_{eff} for null geodesics with $L = 1$ and $M = 1$. (a) Varying $\alpha \in \{0.0, 0.1, 0.2, 0.3, 0.4\}$ at fixed $a = 0.5$. (b) Varying $a \in \{0.3, 0.5, 0.7, 0.9, 1.0\}$ at fixed $\alpha = 0.1$. The peak location corresponds to the PS radius r_{ps} .

3.2 Vacuum Shadow

For an observer located at spatial infinity, the apparent size of the BH shadow is determined by photons that asymptotically approach the PS [42, 79, 80]. The shadow radius, which represents the critical impact parameter separating captured and scattered photon trajectories, is given by

$$R_{sh} = \frac{r_{ps}}{\sqrt{f(r_{ps})}} \sqrt{1 - \alpha} = r_{ps} \sqrt{\frac{1 - \alpha}{f(r_{ps})}}. \quad (16)$$

The factor $\sqrt{1 - \alpha}$ accounts for the redshift correction due to the CoS at the observer's location [47]. In the Schwarzschild limit, we recover $R_{sh}^{\text{Sch}} = 3\sqrt{3}M \approx 5.196M$.

The numerical values of the PS and shadow radii are presented in Table 2 for various combinations of α and a . Both r_{ps} and R_{sh} increase monotonically with increasing α and a . Physically, the CoS reduces the effective gravitational attraction, causing the PS to expand outward. Similarly, increasing a (which corresponds to weaker electromagnetic corrections) allows the spacetime to approach the pure Letelier geometry, which has a larger PS than the electromagnetically modified case.

Figure 4 illustrates the parametric dependence of the shadow radius. In panel (a), R_{sh} is plotted against α for different values of a . All curves exhibit a monotonic increase with α , and for $\alpha > 0$, all curves lie above the Schwarzschild reference line (gray dashed). The curves are approximately parallel, indicating that the CoS and EMU effects contribute additively to the shadow enlargement. In panel (b), R_{sh} is plotted against a for different values of α . The shadow radius increases with a , approaching the Schwarzschild value at $a = 1$ for $\alpha = 0$. Higher values of α shift the entire curve upward, confirming that both parameters independently contribute to shadow expansion.

3.3 Optical Appearance and Emission Decomposition

The visual appearance of a BH depends not only on the shadow size but also on the emission profile of the surrounding accretion environment. Following the methodology employed in the EHT observations [4, 5], we decompose the total observed intensity into three distinct contributions [43, 61]. The direct emission consists of light rays that travel directly from the emitting region to the observer without significant gravitational deflection, contributing to the broad, diffuse glow surrounding the shadow. The lensed emission arises from light rays that undergo moderate gravitational bending, typically completing less than one orbit around the BH before reaching the observer, forming a secondary ring structure outside the PR. The PR contribution comes from light rays that pass very close to the PS, completing one or more half-orbits before escaping, forming a sharp, bright ring at the edge of the shadow that carries information about the strong-field geometry [81].

The observed intensity can be modeled as

$$I_{\text{obs}}(x, y) = I_{\text{direct}}(x, y) + I_{\text{lensed}}(x, y) + I_{\text{ring}}(x, y), \quad (17)$$

where (x, y) are celestial coordinates on the observer's screen. For a geometrically thin, optically thin accretion disk, each component can be approximated by Gaussian profiles centered at characteristic radii determined by the BH geometry [82].

Figure 5 displays the three emission components for varying CoS parameter α at fixed $a = 1$. The rows correspond to $\alpha = 0, 0.1, 0.2$, while the columns show the direct emission, lensed emission, and PR contributions, respectively. The direct emission exhibits a broad intensity distribution peaking outside the shadow boundary, and as

α	$a = 0.5$		$a = 0.8$		$a = 1.0$	
	r_{ps}/M	R_{sh}/M	r_{ps}/M	R_{sh}/M	r_{ps}/M	R_{sh}/M
0.00	2.3660	4.4036	2.7370	4.8587	3.0000	5.1962
0.05	2.5351	4.6882	2.8962	5.1335	3.1579	5.4698
0.10	2.7208	5.0025	3.0730	5.4389	3.3333	5.7735
0.15	2.9264	5.3518	3.2704	5.7801	3.5294	6.1129
0.20	3.1559	5.7431	3.4923	6.1636	3.7500	6.4952
0.25	3.4142	6.1848	3.7435	6.5979	4.0000	6.9282
0.30	3.7078	6.6878	4.0305	7.0945	4.2857	7.4228

Table 2: PS radius r_{ps}/M and shadow radius R_{sh}/M for the Letelier BH in EMU. The Schwarzschild reference values are $r_{ps}^{\text{Sch}} = 3M$ and $R_{sh}^{\text{Sch}} = 3\sqrt{3}M \approx 5.196M$.

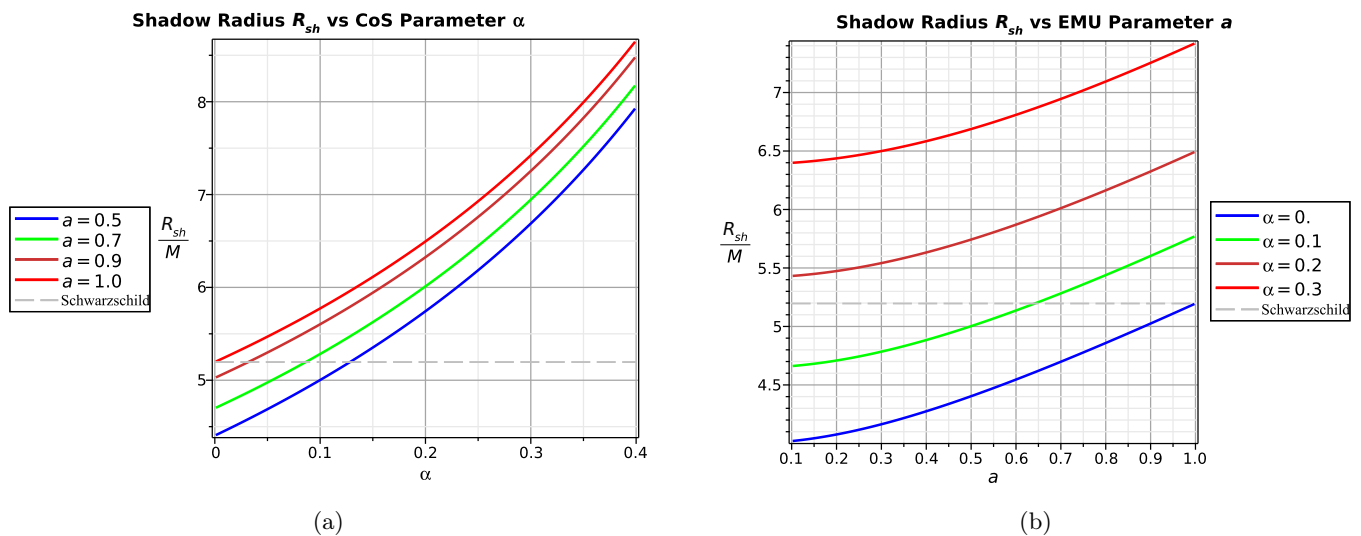


Figure 4: Shadow radius R_{sh}/M as a function of the model parameters. (a) R_{sh} versus CoS parameter α for different values of a . (b) R_{sh} versus EMU parameter a for different values of α . The gray dashed line indicates the Schwarzschild value $R_{sh}^{\text{Sch}} = 3\sqrt{3}M$.

α increases, the shadow region expands and the emission peak shifts outward, consistent with the enlarged PS. The lensed emission forms a narrower ring structure compared to the direct emission, with the ring radius increasing with α to track the PS expansion. The PR appears as a sharp, thin ring at the shadow boundary, representing the most sensitive probe of the near-horizon geometry, and shows clear expansion with increasing α .

3.4 Shadow Images: Parameter Space Exploration

To provide a broad view of the optical appearance across the parameter space, we present in Figure 6 the total intensity maps for nine combinations of (α, a) . The rows correspond to $\alpha = 0, 0.1, \text{ and } 0.2$, while the columns correspond to $a = 0.5, 0.7, \text{ and } 1.0$. The total intensity in-

cludes all three emission components (direct, lensed, and PR) combined.

Several trends are evident in this parameter space exploration. Moving from left to right across each row (increasing a), the shadow size increases, confirming that weaker electromagnetic corrections result in larger shadows, consistent with the analytical predictions in Table 2. Moving from top to bottom in each column (increasing α), the shadow size also increases, demonstrating that the CoS parameter has a pronounced effect on the shadow expansion, with $\alpha = 0.2$ producing noticeably larger shadows than $\alpha = 0$.

The combined effects of both parameters are clearly visible in Figure 6. The largest shadow appears at $(\alpha = 0.2, a = 1.0)$ in the bottom-right panel, while the smallest shadow corresponds to $(\alpha = 0, a = 0.5)$ in the top-left panel. The ratio of shadow radii between these extreme

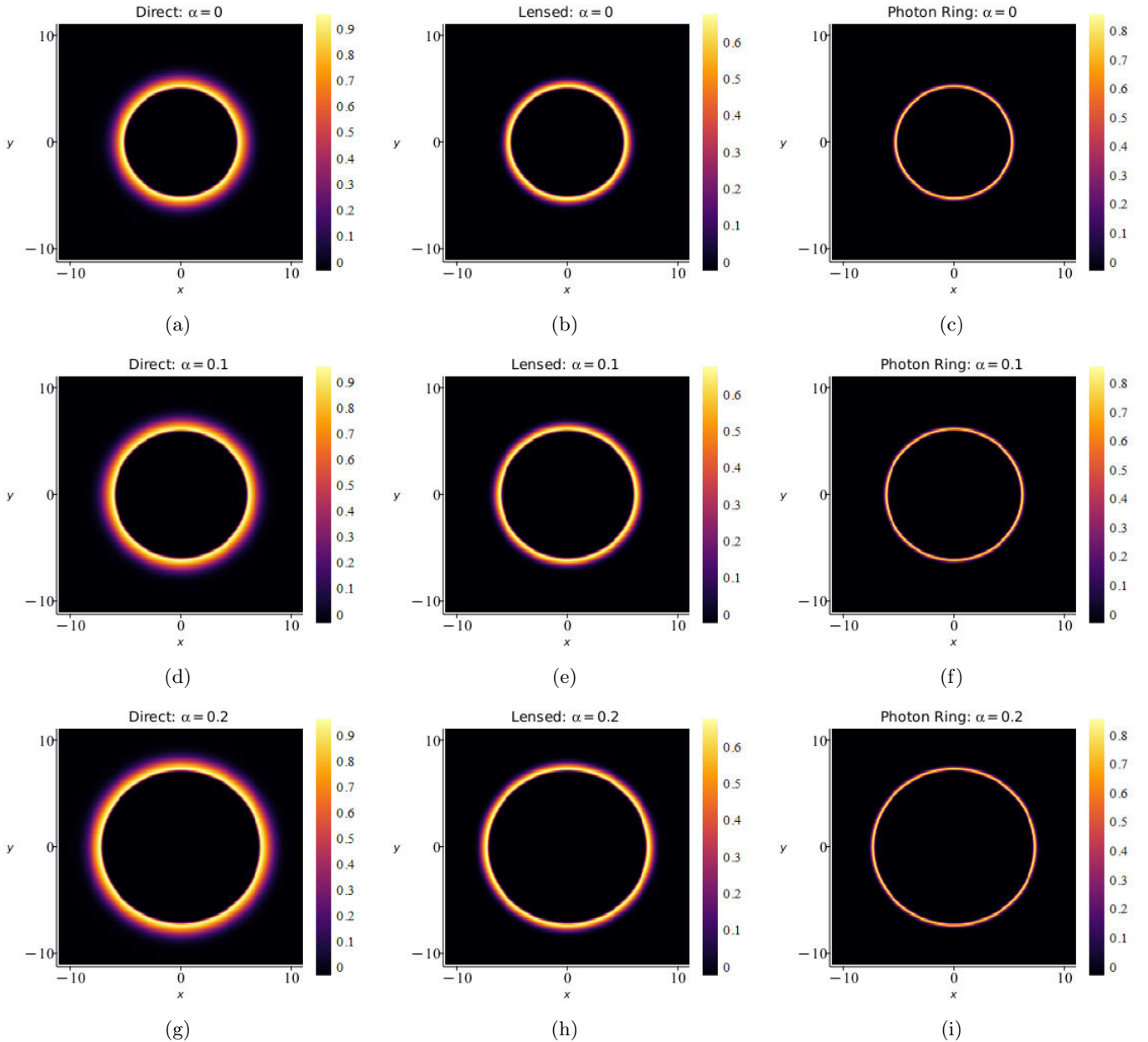


Figure 5: Decomposition of the observed emission into direct, lensed, and PR contributions for varying CoS parameter α at fixed $a = 1$. Top row: $\alpha = 0$ (Schwarzschild limit). Middle row: $\alpha = 0.1$. Bottom row: $\alpha = 0.2$. Left column: direct emission. Middle column: lensed emission. Right column: PR. The shadow size increases with α in all three components, reflecting the expansion of the PS due to the CoS.

cases is approximately $R_{sh}(\alpha = 0.2, a = 1.0)/R_{sh}(\alpha = 0, a = 0.5) \approx 6.50/4.40 \approx 1.48$, representing a 48% increase in apparent size. The bright PR at the shadow boundary remains visible across all parameter combinations, though its radius varies with the parameters. The ring brightness relative to the background emission is relatively insensitive to the parameter values, suggesting that the PR contrast is a feature of the Letelier BH in EMU.

3.5 Shadow in Homogeneous Plasma

We now consider the BH immersed in a homogeneous plasma with constant plasma frequency ω_p [48, 83]. The refractive index of the plasma is given by

$$n^2(r) = 1 - \frac{\omega_p^2}{\omega^2}, \quad (18)$$

where ω is the photon frequency measured by a static observer. In the presence of plasma, the photon trajectories are modified due to the dispersive nature of the medium [84]. The modified effective potential for photon motion

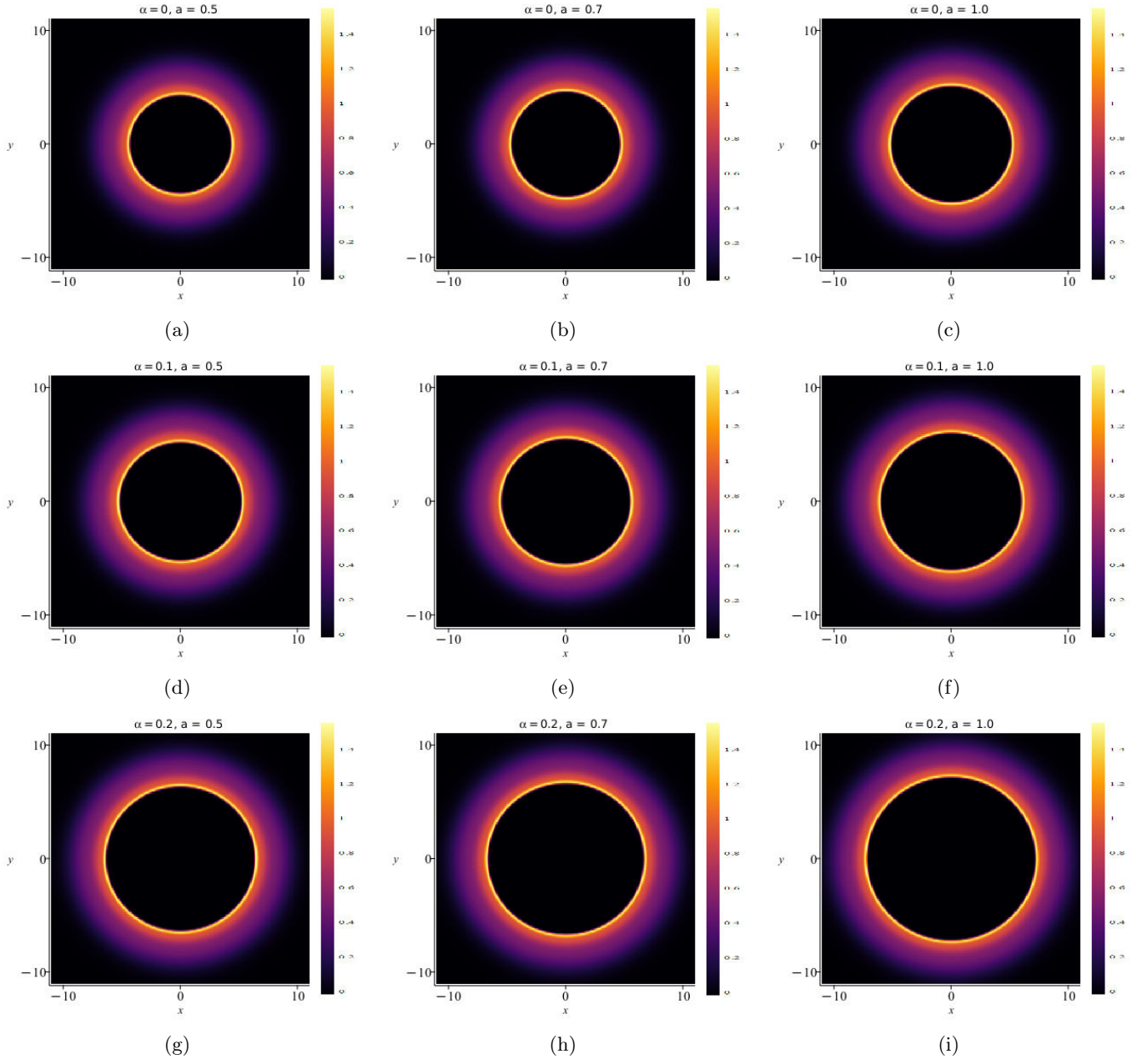


Figure 6: Shadow images of the Letelier BH in EMU across the parameter space. Top row: $\alpha = 0$. Middle row: $\alpha = 0.1$. Bottom row: $\alpha = 0.2$. Left column: $a = 0.5$. Middle column: $a = 0.7$. Right column: $a = 1.0$. The total intensity includes direct emission, lensed emission, and PR contributions. The shadow size increases with both α and a , with the largest shadow at $(\alpha = 0.2, a = 1.0)$ and the smallest at $(\alpha = 0, a = 0.5)$.

becomes

$$V_{\text{eff}}^{(\text{pl})} = f(r) \left(\frac{L^2}{r^2} + \omega_p^2 \right) - E^2, \quad (19)$$

where E is the conserved photon energy. Introducing the dimensionless plasma parameter $k = \omega_p^2 / \omega_\infty^2$, where ω_∞ is the photon frequency at infinity, the PS condition becomes

$$(1 + k)r f'(r_{ps}) - 2f(r_{ps}) = 0. \quad (20)$$

This modified condition shows that the plasma effectively increases the “centrifugal” contribution, shifting the PS outward for $k > 0$.

The corresponding shadow radius in the plasma environment is

$$R_{sh}^{(\text{pl})} = r_{ps} \sqrt{\frac{(1 - \alpha)(1 - kf(r_{ps}))}{f(r_{ps})}}. \quad (21)$$

The factor $(1 - kf(r_{ps}))$ under the square root arises from the plasma dispersion relation and is responsible for the shadow size reduction in the presence of plasma.

Table 3 presents the shadow radius for various plasma concentrations at fixed $\alpha = 0.1$. The plasma effect reduces the shadow size, with stronger reduction at higher plasma

density. At $k = 0.4$, the shadow radius decreases by approximately 5% compared to the vacuum case. This reduction occurs because the effective refractive index $n < 1$ in the plasma causes photons to bend less strongly than in vacuum, allowing more photons to escape rather than being captured [85].

k	$a = 0.5$	$a = 0.7$	$a = 0.9$	$a = 1.0$
0.00	5.0025	5.2829	5.6031	5.7735
0.10	4.9391	5.2116	5.5233	5.6892
0.20	4.8791	5.1431	5.4456	5.6068
0.30	4.8191	5.0738	5.3663	5.5225
0.40	4.7560	5.0008	5.2827	5.4334

Table 3: Shadow radius $R_{sh}^{(pl)}/M$ in homogeneous plasma for $\alpha = 0.1$. Here $k = \omega_p^2/\omega_\infty^2$ is the plasma parameter.

3.6 Shadow in Inhomogeneous Plasma

For a more realistic astrophysical scenario, we consider an inhomogeneous plasma with a power-law density profile [86, 87]

$$\omega_p^2(r) = \frac{\omega_c^2}{r^q}, \quad (22)$$

where ω_c is a characteristic plasma frequency and q determines the radial falloff. The case $q = 1$ corresponds to spherical accretion onto the BH, which is relevant for low-luminosity AGN and the Galactic Center environment surrounding Sgr A* [88].

Defining the inhomogeneous plasma parameter $k_c = \omega_c^2/\omega_\infty^2$, the modified PS condition for $q = 1$ reads

$$(r + k_c)f'(r_{ps}) - 2f(r_{ps}) = 0. \quad (23)$$

The refractive index at the PS becomes

$$n^2(r_{ps}) = 1 - \frac{k_c f(r_{ps})}{r_{ps}}, \quad (24)$$

and the shadow radius is

$$R_{sh}^{(pl)} = r_{ps} \sqrt{\frac{(1 - \alpha)n^2(r_{ps})}{f(r_{ps})}}. \quad (25)$$

The results for inhomogeneous plasma are presented in Table 4. Comparing with Table 3, we observe that the inhomogeneous plasma has a weaker effect on the shadow size than the homogeneous case at comparable parameter values. For example, at $k_c = 0.20$, the shadow radius decreases by only about 1% compared to vacuum, whereas the homogeneous plasma with $k = 0.20$ produces a 2.5% reduction. This difference is expected since the plasma density $\omega_p^2(r) \propto 1/r$ falls off with distance, concentrating the plasma influence in the immediate vicinity of the BH where its effect on photon trajectories is less cumulative.

k_c	$a = 0.5$	$a = 0.7$	$a = 0.9$	$a = 1.0$
0.00	5.0025	5.2829	5.6031	5.7735
0.05	4.9904	5.2705	5.5904	5.7607
0.10	4.9788	5.2584	5.5779	5.7480
0.15	4.9676	5.2467	5.5657	5.7356
0.20	4.9566	5.2352	5.5538	5.7235

Table 4: Shadow radius $R_{sh}^{(pl)}/M$ in inhomogeneous plasma ($q = 1$) for $\alpha = 0.1$. Here $k_c = \omega_c^2/\omega_\infty^2$ is the inhomogeneous plasma parameter.

3.7 Photon Trajectories

To visualize the light deflection near the Letelier BH in EMU, we numerically integrate the photon orbit equation [89]. For a photon with impact parameter b , the orbit in the (r, ϕ) plane satisfies

$$\left(\frac{dr}{d\phi}\right)^2 = r^4 \left(\frac{1}{b^2} - \frac{f(r)}{r^2}\right). \quad (26)$$

The critical impact parameter $b_{cr} = r_{ps}/\sqrt{f(r_{ps})}$ separates captured trajectories ($b < b_{cr}$) from scattered ones ($b > b_{cr}$). For photons with $b = b_{cr}$, the trajectory asymptotically approaches the PS, where the photon can orbit indefinitely in an unstable circular orbit.

Figure 7 displays representative photon trajectories for different impact parameters at $\alpha = 0.1$ and $a = 0.5$. The trajectories are labeled by the ratio b/b_{cr} , allowing direct comparison of the deflection behavior relative to the critical case. Photons with $b/b_{cr} < 1$ are captured by the BH, spiraling into the EH after multiple orbits near the PS. The number of orbits before capture increases as b approaches b_{cr} from below.

Photons with $b/b_{cr} > 1$ are scattered to infinity after experiencing gravitational deflection. The deflection angle decreases as b/b_{cr} increases, ranging from near-infinite deflection at the critical value to weak-field bending for $b/b_{cr} \gg 1$. The critical trajectory ($b/b_{cr} = 1$) represents the boundary between capture and scattering, corresponding to photons that asymptotically approach the PS.

The golden ring in Figure 7 indicates the PS at $r_{ps} = 2.72M$, while the black disk represents the EH at $r_+ = 1.74M$. The four-fold symmetry of the trajectory pattern reflects the spherical symmetry of the spacetime, with incoming photons from all directions experiencing equivalent gravitational deflection.

3.8 Observational Implications and EHT Constraints

The results presented in this section have several implications for current and future BH observations. The EHT

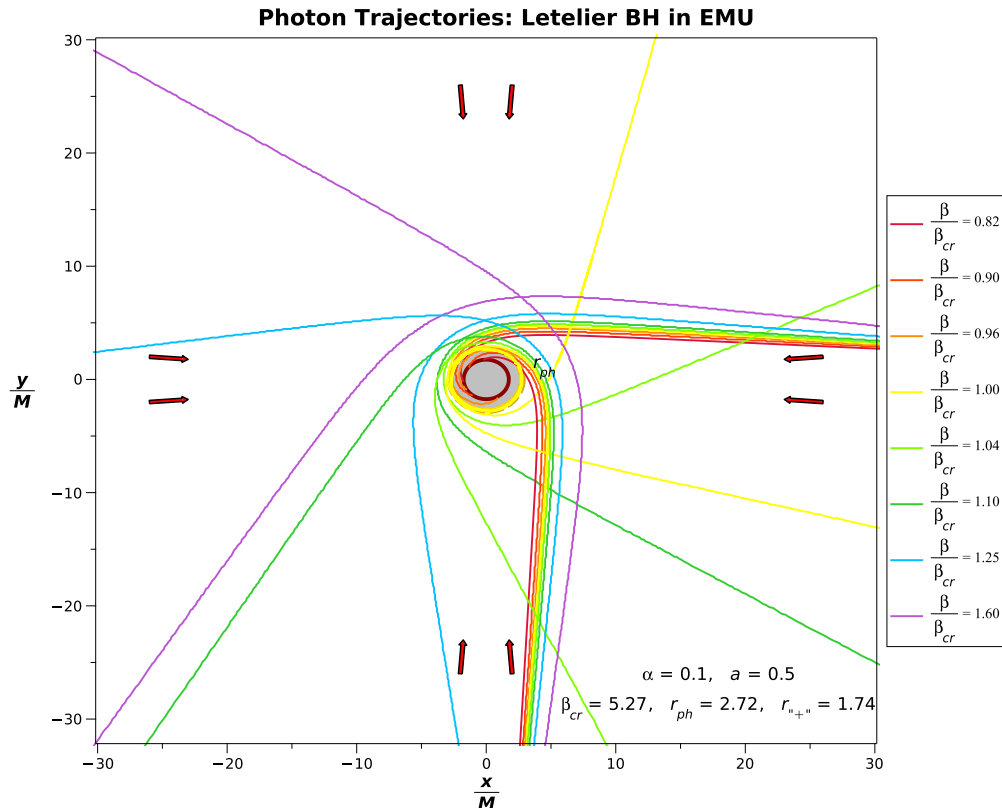


Figure 7: Photon trajectories around the Letelier BH in EMU for $\alpha = 0.1$ and $a = 0.5$. The trajectories are labeled by the ratio b/b_{cr} , where $b_{cr} = 5.27M$ is the critical impact parameter. The golden ring indicates the PS at $r_{ps} = 2.72M$, and the black disk represents the EH at $r_+ = 1.74M$. Captured trajectories ($b < b_{cr}$) spiral into the BH, while deflected trajectories ($b > b_{cr}$) escape to infinity.

observations of M87* and Sgr A* have provided measurements of the shadow size with approximately 10% precision [4, 5]. The variation of R_{sh} with α and a shown in Table 2 suggests that constraints on these parameters could be derived from shadow size measurements. For example, a shadow 20% larger than Schwarzschild would be consistent with $\alpha \approx 0.15$ at $a = 1$.

Future space-based VLBI observations with improved resolution may directly resolve the PR structure [61, 90]. The decomposition shown in Figure 5 demonstrates that the PR is a remarkable feature across the parameter space, though its radius varies with α and a . For observations at lower frequencies where plasma effects become significant, Tables 3 and 4 provide predictions for the shadow size modification. The relatively weak dependence on plasma parameters suggests that plasma corrections are subdominant to the geometric effects of α and a for typical astrophysical environments.

The similar effects of α and a on the shadow size may lead to degeneracies in parameter estimation from shadow observations alone. Breaking these degeneracies may require complementary information from PR subrings, GW observations, or stellar dynamics in the vicinity of the BH [91, 92]. Additionally, the ngEHT and proposed space missions offer the prospect of measuring the PR with sufficient

precision to distinguish between different BH models [93]. The detailed predictions provided in this section, particularly the emission decomposition and parameter space exploration, will be valuable for interpreting such future observations in the context of the Letelier BH in EMU.

4 HR and Energy Emission

In this section, we investigate the HR properties of the Letelier BH in EMU. We derive the Hawking temperature and analyze the energy emission rate, which depends on both the CoS parameter α and the EMU parameter a . The radiation spectra for different spin fields, including scalar ($s = 0$), EM ($s = 1$), and Dirac ($s = 1/2$) fields, are computed and compared with the Schwarzschild case.

4.1 Hawking Temperature

The Hawking temperature for the Letelier BH in EMU was derived in Sec. 2 from the surface gravity at the outer horizon. Recalling Eq. (12), we have

$$T_H = \frac{(1 - \alpha)\sqrt{1 - (1 - \alpha)(1 - a^2)}}{4\pi M}, \quad (27)$$

which reduces to the Schwarzschild value $T_H^{\text{Sch}} = 1/(8\pi M)$ in the limit $\alpha = 0$, $a = 1$.

Table 5 presents the normalized Hawking temperature T_H/T_H^{Sch} for various combinations of α and a . The temperature decreases monotonically with increasing α , reflecting the gravitational dilution caused by the CoS. At $\alpha = 0.3$, the temperature is reduced to approximately half of the Schwarzschild value. The dependence on the EMU parameter a is weaker but still significant, with smaller values of a (stronger EM corrections) leading to slightly lower temperatures. The physical interpretation is that the CoS effectively increases the horizon radius for a given mass, thereby reducing the surface gravity and hence the temperature [94, 95].

α	$a = 0.5$	$a = 0.7$	$a = 0.9$	$a = 1.0$
0.00	0.8889	0.9689	0.9972	1.0000
0.05	0.8202	0.8782	0.9003	0.9025
0.10	0.7493	0.7912	0.8082	0.8100
0.15	0.6779	0.7081	0.7211	0.7225
0.20	0.6076	0.6291	0.6389	0.6400
0.25	0.5391	0.5544	0.5617	0.5625
0.30	0.4734	0.4841	0.4894	0.4900

Table 5: Normalized Hawking temperature T_H/T_H^{Sch} for the Letelier BH in EMU, where $T_H^{\text{Sch}} = 1/(8\pi M)$ is the Schwarzschild temperature.

4.2 Total Emission Power

The total power emitted by the BH is obtained by integrating the energy emission rate over all frequencies [96]. In the Stefan-Boltzmann approximation, the total power scales as

$$P = \sigma_{\text{SB}} A_{\text{eff}} T_H^4, \quad (28)$$

where σ_{SB} is the Stefan-Boltzmann constant and $A_{\text{eff}} = 27\pi R_{sh}^2$ is the effective emission area in the geometric optics limit [97]. This expression shows that the total power depends on both the shadow radius and the fourth power of the temperature, making it highly sensitive to the BH parameters.

Figure 8 presents the normalized total emission power P/P_{Sch} as a function of the model parameters. Panel (a) shows the power versus α for different values of a . All curves decrease monotonically with increasing α , reflecting the combined effect of reduced temperature and modified shadow radius. The suppression is dramatic: at $\alpha = 0.3$, the power is reduced to approximately 10–15% of the Schwarzschild value regardless of a . The curves for different a values are well separated at small α but converge at large α , indicating that the CoS effect dominates over the EMU correction in the strong- α regime.

Panel (b) displays the power versus a for different values of α . All curves increase with increasing a , confirming that weaker EMU corrections lead to higher emission rates. The $\alpha = 0$ curve reaches unity at $a = 1$, corresponding to the Schwarzschild limit. For $\alpha = 0.3$, the power remains below 0.15 across the entire range of a , demonstrating the strong suppression effect of the CoS.

4.3 HR Spectra for Different Spin Fields

The HR spectrum depends on the spin of the emitted particles through both the statistical distribution and the greybody factors [56, 98]. The particle emission rate for a field of spin s is given by

$$\frac{d^2 N_s}{d\omega dt} = \frac{1}{2\pi} \sum_{\ell} \frac{(2\ell + 1) \mathcal{T}_s(\omega, \ell)}{\exp(\omega/T_H) - (-1)^{2s}}, \quad (29)$$

where $\mathcal{T}_s(\omega, \ell)$ is the greybody factor for mode ℓ and the sign in the denominator distinguishes bosons ($-$) from fermions ($+$) [99]. The energy emission rate is $d^2 E_s/d\omega dt = \omega \cdot d^2 N_s/d\omega dt$.

Figure 9 compares the energy spectra for scalar ($s = 0$), EM ($s = 1$), and Dirac ($s = 1/2$) fields. The solid curves correspond to the Schwarzschild case ($\alpha = 0$, $a = 1$), while the dashed curves represent the Letelier BH in EMU ($\alpha = 0.1$, $a = 0.8$). For the Schwarzschild BH, the EM field exhibits the highest emission rate with a peak of approximately 0.022 at $\omega M \approx 0.09$, followed by the Dirac field with peak ~ 0.013 and the scalar field with peak ~ 0.012 . This hierarchy reflects the different numbers of degrees of freedom: the EM field has 2 polarizations, while the Dirac field has 4 spinor components (weighted by 7/8 due to Fermi-Dirac statistics) [100]. Comparing the Letelier-EMU case to Schwarzschild, the peak heights are reduced by approximately 39%, 45%, and 38% for scalar, EM, and Dirac fields, respectively. In all cases, the peak shifts to lower frequencies, consistent with the reduced Hawking temperature. The EM field shows the largest relative suppression, indicating that the greybody factors for higher-spin fields are more sensitive to the spacetime geometry modifications [59].

The total power emitted in each spin channel is obtained by integrating the energy spectrum over all frequencies [101]. In the Stefan-Boltzmann approximation, the power scales as $P_s \propto g_s R_{sh}^2 T_H^4$, where g_s is the effective number of degrees of freedom: $g_{s=0} = 1$ for scalars, $g_{s=1} = 2$ for EM fields, and $g_{s=1/2} = 7/2$ for Dirac fields (accounting for 4 spinor components with the fermionic factor 7/8) [102].

Table 6 presents the total power for each spin channel at two representative values of the EMU parameter. The ratio $P_{s=1}/P_{s=0} = 2$ is maintained across all parameter values, confirming the expected scaling with degrees of freedom. Similarly, $P_{s=1/2}/P_{s=0} \approx 3.5$ reflects the fermionic degrees of freedom. The total power decreases significantly with increasing α : at $\alpha = 0.20$, the emission is reduced to approximately 25–35% of the $\alpha = 0$ value

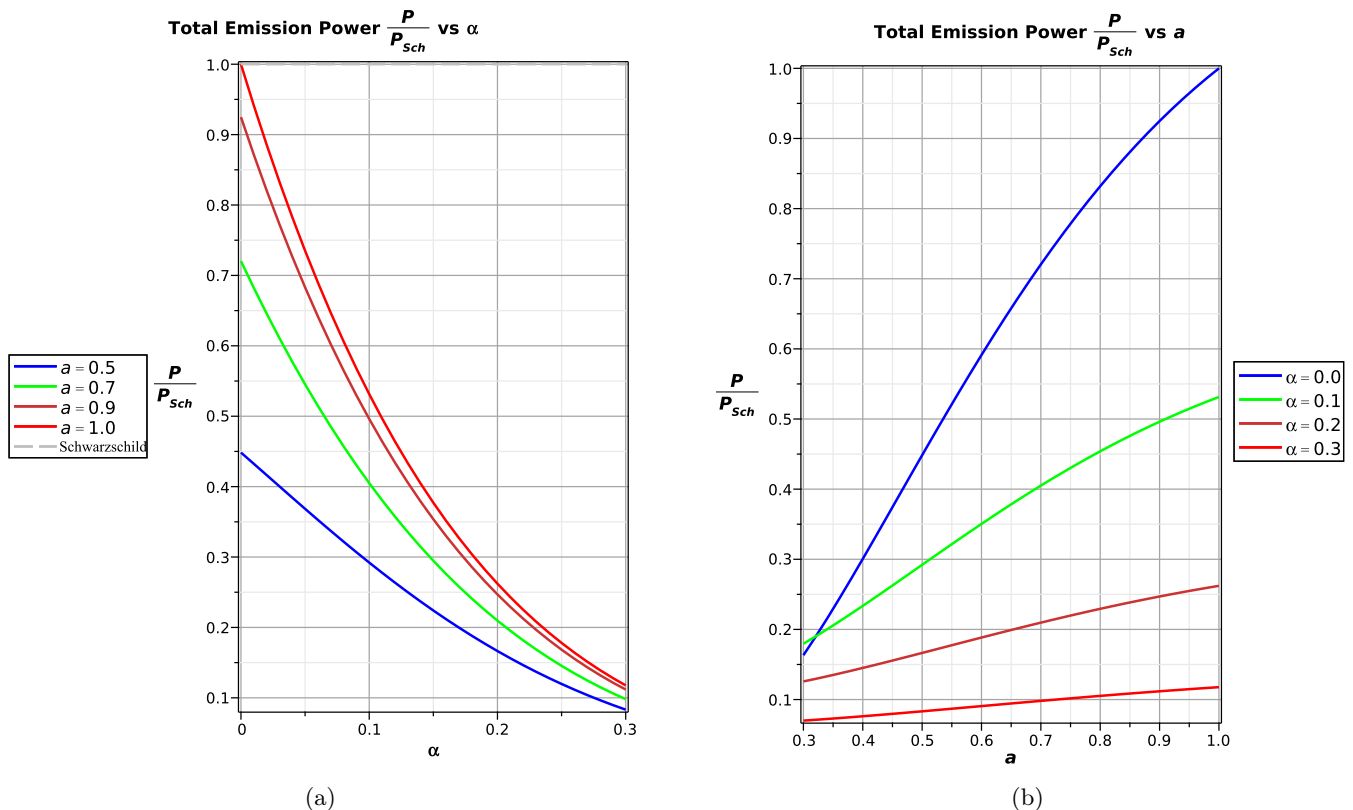


Figure 8: Normalized total emission power P/P_{Sch} for the Letelier BH in EMU. (a) Power versus CoS parameter α for different values of a . The gray dashed line indicates the Schwarzschild reference P_{Sch} . (b) Power versus EMU parameter a for different values of α . The power decreases with increasing α and increases with increasing a .

for both $a = 0.5$ and $a = 1.0$. The EMU parameter also affects the emission, with $a = 1.0$ giving roughly twice the power of $a = 0.5$ at the same α .

The results presented in this section have important implications for BH evaporation in the presence of a CoS and EMU corrections [103, 104]. The reduced Hawking temperature implies a longer evaporation timescale, since the mass loss rate scales as $dM/dt \propto -T_H^4$ [105]. For a Letelier BH in EMU with $\alpha = 0.2$, the evaporation rate is suppressed by a factor of $(0.64)^4 \approx 0.17$ compared to Schwarzschild, leading to an evaporation time approximately 6 times longer.

The modification of the HR spectrum also affects the particle content of the emitted radiation. The shift of the peak to lower frequencies means that the typical energy of emitted particles is reduced, which may have consequences for observational signatures of primordial BH evaporation [106?]. Furthermore, the relative contributions of different spin channels remain approximately constant across the parameter space, suggesting that the particle ratios in HR are special features determined primarily by the degrees of freedom rather than the specific BH geometry.

From an observational perspective, the suppression of HR by the CoS could explain why primordial BHs with masses in the asteroid range (10^{15} – 10^{18} g) might still survive to the present day if they were formed in an environment with significant string density [107]. The EMU

corrections provide an additional mechanism for modulating the evaporation rate, offering a rich phenomenology for constraining these parameters through observations of the diffuse gamma-ray background or direct searches for evaporating BHs [108, 109]. Future gamma-ray observatories such as the Cherenkov Telescope Array (CTA) may provide improved sensitivity to the HR signatures from primordial BHs, enabling constraints on the CoS and EMU parameters in the early universe [110].

5 Phase Structure and JTE with Barrow Entropy

Barrow introduced a modification of BH entropy by suggesting that quantum-gravitational effects may deform the horizon geometry itself, leading to an effectively fractal surface rather than a smooth manifold [111, 112]. In this approach, the horizon entropy is generalized to the Barrow entropy, expressed as

$$S_B = (\pi r_+^2)^{1+\frac{\Delta}{2}}, \quad (30)$$

where the parameter $\Delta \in [0, 1]$ characterizes the extent of geometric deformation [38]. The classical Bekenstein–Hawking area law is recovered when $\Delta = 0$, corresponding to an undeformed, smooth horizon, while $\Delta = 1$ repre-

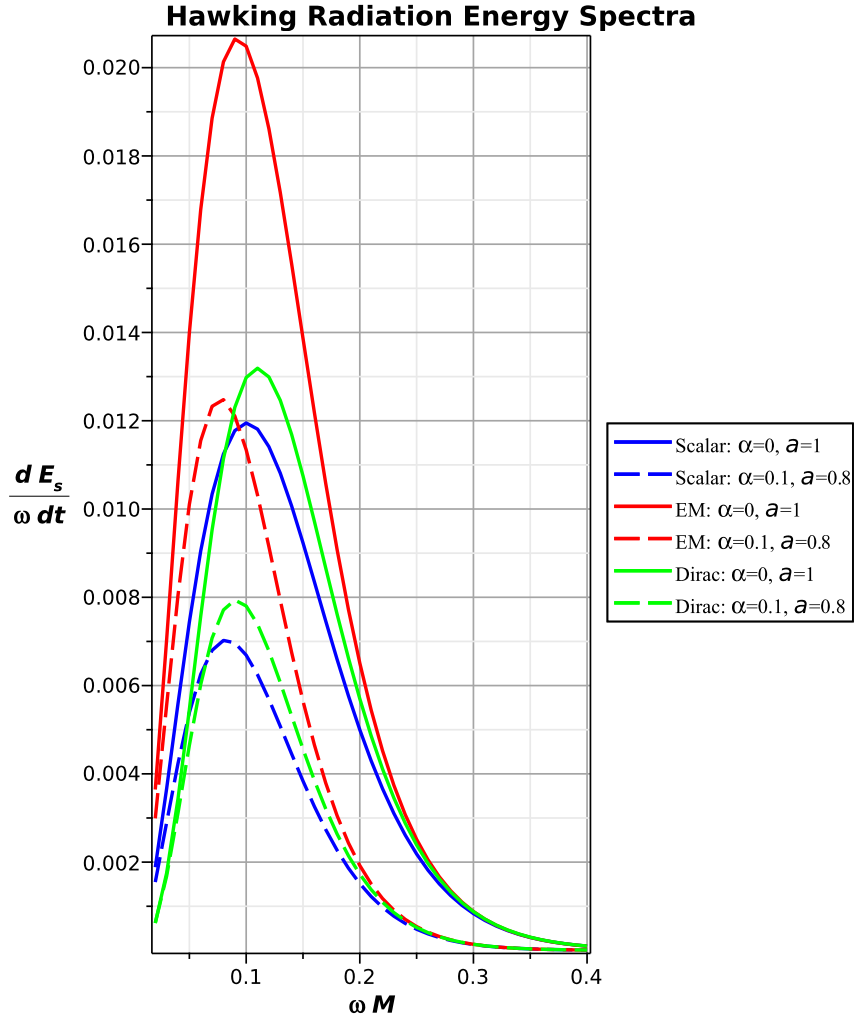


Figure 9: Comparison of HR energy spectra for scalar (blue), EM (red), and Dirac (green) fields from the Letelier BH in EMU. Solid curves: Schwarzschild limit ($\alpha = 0$, $a = 1$). Dashed curves: Letelier BH in EMU ($\alpha = 0.1$, $a = 0.8$). The EM field exhibits the highest emission rate, followed by Dirac and scalar fields.

α	$a = 0.5$			$a = 1.0$		
	$P_{s=0}$	$P_{s=1}$	$P_{s=1/2}$	$P_{s=0}$	$P_{s=1}$	$P_{s=1/2}$
0.00	42.34	84.67	148.2	94.42	188.8	330.5
0.05	34.79	69.58	121.8	69.41	138.8	242.9
0.10	27.58	55.16	96.54	50.18	100.4	175.6
0.15	21.16	42.31	74.05	35.61	71.22	124.6
0.20	15.72	31.43	55.01	24.75	49.50	86.63

Table 6: Total HR power (in units of $10^{-5}/M^2$) for scalar ($s = 0$), EM ($s = 1$), and Dirac ($s = 1/2$) fields from the Letelier BH in EMU.

sents the extreme case in which the horizon exhibits maximal fractal irregularity. Unlike entropy corrections derived from statistical fluctuations or ensemble considerations [113, 114], the Barrow entropy has a fundamentally geometric origin. As such, it is expected to encode certain

aspects of quantum gravity related to microscopic spacetime structure, possibly associated with spacetime foam or loop quantum gravity-inspired effects at small length scales [115, 116].

The Barrow entropy framework has attracted consid-

erable attention in cosmological contexts, where it modifies the Friedmann equations and leads to observable deviations from standard Λ CDM predictions [40, 117]. For BH thermodynamics, the Barrow modification alters the entropy-area relation and consequently affects all derived thermodynamic quantities, including the heat capacity, free energy, and phase transition structure [41].

5.1 Heat Capacity and Thermodynamic Stability

To investigate the thermodynamic stability and phase behavior of the Letelier BH in EMU within this framework, we analyze the heat capacity constructed from the Barrow entropy. For fixed thermodynamic volume, the heat capacity is defined by [118, 119]

$$C_B = T_H \left(\frac{\partial S_B}{\partial T_H} \right)_V, \quad (31)$$

which, upon substituting the explicit expressions for the Hawking temperature from Eq. (27) and the horizon radius from Eq. (4), leads to

$$C_B = - \frac{\pi^{1+\frac{\Delta}{2}} r_+^2 (2 + \Delta) (r_+^2)^{\frac{\Delta}{2}} (Ma^2 - M + r_+)}{3Ma^2 - 3M + 2r_+}. \quad (32)$$

The qualitative behavior of the heat capacity plays a decisive role in identifying locally stable and unstable thermodynamic regions [120]. In particular, divergences of C_B signal the presence of second-order phase transitions, while changes in its sign distinguish between stable ($C_B > 0$) and unstable ($C_B < 0$) branches of the BH configuration [121].

The denominator of Eq. (32) vanishes when

$$r_+^{\text{crit}} = \frac{3M(1 - a^2)}{2}, \quad (33)$$

which defines the critical horizon radius at which the heat capacity diverges. This divergence marks a second-order phase transition between small and large BH branches. For $r_+ < r_+^{\text{crit}}$, the heat capacity is negative, indicating thermodynamic instability, while for $r_+ > r_+^{\text{crit}}$, the heat capacity becomes positive, corresponding to a locally stable configuration.

The Barrow parameter Δ modifies the magnitude of C_B through the prefactor $(2 + \Delta)$ and the power-law dependence $(r_+^2)^{\Delta/2}$, but does not alter the location of the phase transition point, which is determined solely by the metric parameters M and a . This observation suggests that the Barrow deformation affects the thermodynamic response but preserves the underlying phase structure dictated by the spacetime geometry.

Figure 10 displays the heat capacity C_B as a function of the horizon radius for selected values of the Barrow parameter Δ at fixed $a = 0.2$ and $M = 1$. The divergence at $r_+^{\text{crit}} \approx 1.44M$ is clearly visible, separating the unstable small-BH branch (left) from the stable large-BH branch

(right). Increasing Δ amplifies the magnitude of C_B in both regions while maintaining the transition point, consistent with the analytical expectation from Eq. (32).

5.2 JTE

We further examine the JTE, which describes the isenthalpic evolution of the BH and provides insight into its heating and cooling properties during expansion processes [122–124]. The JTE has emerged as a powerful tool for probing BH thermodynamics in extended phase space, where the cosmological constant is interpreted as thermodynamic pressure [75, 125].

The Joule–Thomson coefficient is defined as [126]

$$\mu_J = \left(\frac{\partial T}{\partial P} \right)_H, \quad (34)$$

where the subscript H denotes constant enthalpy (mass). When evaluated in the Barrow entropy scenario for the Letelier BH in EMU, it takes the form

$$\mu_J = \frac{12r_+ (Ma^2 - M + \frac{2}{3}r_+) (r_+^2)^{-\frac{\Delta}{2}} \pi^{-\frac{\Delta}{2}}}{(3Ma^2 - 3M + 2r_+) \Delta - 12Ma^2 + 12M - 6r_+}. \quad (35)$$

The sign of μ_J determines the thermodynamic response of the BH under expansion: positive values ($\mu_J > 0$) correspond to cooling, whereas negative values ($\mu_J < 0$) indicate heating [127]. The inversion temperature T_i , at which $\mu_J = 0$, separates the cooling and heating regimes and is obtained from the condition

$$Ma^2 - M + \frac{2}{3}r_+ = 0 \quad \Rightarrow \quad r_+^{\text{inv}} = \frac{3M(1 - a^2)}{2}. \quad (36)$$

Interestingly, the inversion radius r_+^{inv} coincides with the critical radius r_+^{crit} from the heat capacity analysis, indicating a deep connection between the phase transition structure and the JTE behavior.

The presence of the Barrow deformation parameter Δ introduces substantial modifications to the JTE coefficient through the factors $(r_+^2)^{-\Delta/2}$ and $\pi^{-\Delta/2}$ in the numerator, as well as the Δ -dependent term in the denominator. These modifications alter the magnitude of μ_J and can shift the positions of additional extrema, thereby affecting the cooling-heating transition dynamics and leading to thermodynamic behavior that deviates from the standard entropy formulation [128].

Figure 11 presents the Joule–Thomson coefficient μ_J as a function of the horizon radius for selected values of Δ at fixed $a = 0.5$ and $M = 1$. The zero crossing at $r_+^{\text{inv}} \approx 1.125M$ marks the inversion point separating the cooling region ($\mu_J > 0$, small r_+) from the heating region ($\mu_J < 0$, large r_+). The Barrow parameter modifies the slope and curvature of the μ_J profile, with larger Δ producing steeper transitions near the inversion point.

The inversion curve in the T – P plane is obtained by plotting the inversion temperature T_i against the corresponding pressure P_i as the horizon radius varies [129].

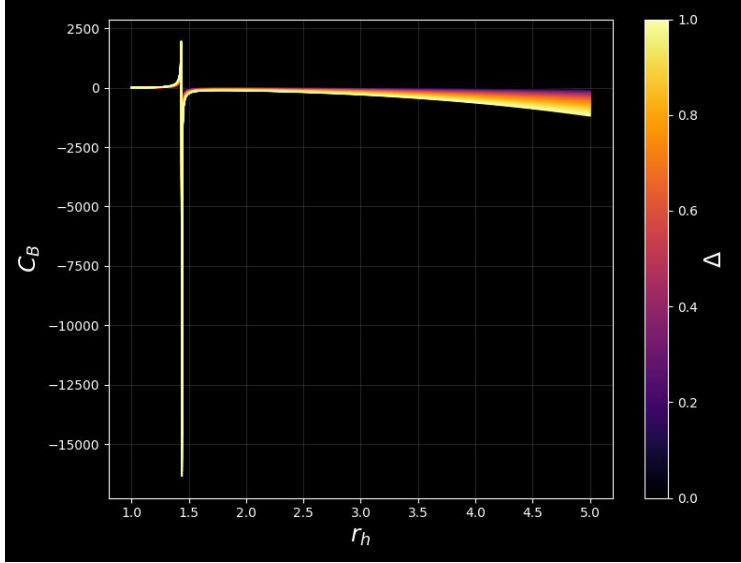


Figure 10: Heat capacity C_B as a function of the horizon radius r_+/M for the Letelier BH in EMU with Barrow entropy. Parameters: $a = 0.2$, $M = 1$, and $\Delta \in \{0, 0.3, 0.6, 1.0\}$. The divergence at $r_+^{\text{crit}} \approx 1.44M$ signals a second-order phase transition. Positive (negative) values indicate thermodynamically stable (unstable) configurations.

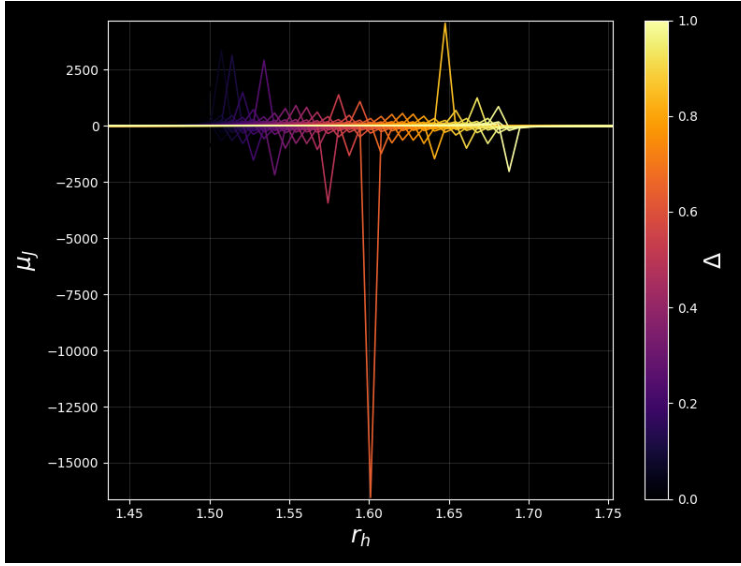


Figure 11: Joule–Thomson coefficient μ_J as a function of the horizon radius r_+/M for the Letelier BH in EMU with Barrow entropy. Parameters: $a = 0.5$, $M = 1$, and $\Delta \in \{0, 0.3, 0.6, 1.0\}$. The zero crossing defines the inversion point r_+^{inv} , separating cooling ($\mu_J > 0$) from heating ($\mu_J < 0$) regimes.

For the Letelier BH in EMU with Barrow entropy, the inversion curve exhibits characteristic features that distinguish it from both the Schwarzschild case and the standard Bekenstein–Hawking entropy formulation. The ratio of minimum inversion temperature to critical temperature, T_i^{min}/T_c , provides a useful diagnostic for comparing different BH systems with van der Waals fluids [130]. For van der Waals fluids, this ratio is approximately 0.5, while for RN-AdS BHs it is exactly 0.5 in the large charge limit. The Barrow modification shifts this ratio, with larger Δ values producing deviations from the standard BH thermodynamics predictions.

Table 7 summarizes the Hawking temperature for representative values of α and a . The inversion radius $r_+^{\text{inv}} = 3M(1 - a^2)/2$ depends only on a and is independent of both α and the Barrow parameter, confirming the geometric origin of the inversion condition. For $a = 0.5$, we obtain $r_+^{\text{inv}}/M = 1.125$, while for $a = 0.8$, the inversion radius shrinks to $r_+^{\text{inv}}/M = 0.540$. The Hawking temperature decreases monotonically with increasing α , reflecting the gravitational dilution caused by the CoS.

The Barrow parameter Δ modifies the magnitude of the JTE coefficient through the factors $(r_+^2)^{-\Delta/2}$ and $\pi^{-\Delta/2}$, but does not affect the inversion radius or the Hawking

α	a	r_+^{inv}/M	$T_H M$
0.00	0.5	1.125	0.0354
0.00	0.8	0.540	0.0393
0.10	0.5	1.125	0.0298
0.10	0.8	0.540	0.0319
0.20	0.5	1.125	0.0242
0.20	0.8	0.540	0.0253

Table 7: Inversion radius and Hawking temperature for the Letelier BH in EMU with $M = 1$. The inversion radius $r_+^{\text{inv}} = 3M(1 - a^2)/2$ is independent of α , while the Hawking temperature T_H decreases with increasing α .

temperature. This separation of scales indicates that the geometric properties of the phase transition (determined by α and a) are distinct from the quantum-gravitational corrections encoded in Δ .

The connection between Barrow entropy and the Letelier-EMU spacetime geometry opens a window into quantum gravity phenomenology [131]. The Barrow parameter Δ encodes information about the fractal dimension of the horizon, which may be constrained through observations of BH thermodynamic properties or cosmological data [132, 133].

The modified phase structure and JTE behavior carry several implications. First, the amplification of the heat capacity magnitude with increasing Δ suggests enhanced thermodynamic response near phase transitions, which could manifest in modified fluctuation spectra for near-critical BHs. Second, the preservation of the critical and inversion radii under Barrow modification indicates that certain geometric features of the phase structure remain stable against quantum-gravitational corrections, pointing toward potential universality classes for BH thermodynamics [134]. Third, the deviation of the T_i^{min}/T_c ratio from the van der Waals value offers a quantitative probe for distinguishing Barrow-modified BHs from their classical counterparts.

6 Dirac Field Perturbations

In this section, we extend the perturbation analysis beyond scalar fields to investigate the propagation of Dirac (spin-1/2) fields in the Letelier BH in EMU background. These perturbations are important for understanding the stability of the BH under different spin fields and provide additional observational signatures through their greybody factors and emission spectra [58, 135].

6.1 Dirac Equation in Curved Spacetime

The dynamics of a massless spin-1/2 field in curved spacetime is described by the Dirac equation [136, 137]

$$\gamma^\mu \nabla_\mu \Psi = 0, \quad (37)$$

where γ^μ are the curved-space gamma matrices satisfying $\{\gamma^\mu, \gamma^\nu\} = 2g^{\mu\nu}$, and ∇_μ is the spinor covariant derivative. Using the Newman-Penrose formalism and separating variables, the Dirac equation in the Letelier-EMU background reduces to two coupled first-order equations [138, 139]. Introducing the tortoise coordinate and eliminating one component, we obtain the Schrödinger-like equation

$$\frac{d^2 \Psi_{\text{D}}^\pm}{dr_*^2} + \left[\omega^2 - V_{\text{eff}}^{(\text{D})\pm}(r) \right] \Psi_{\text{D}}^\pm = 0, \quad (38)$$

where the effective potentials for the two chiralities are given by [140]

$$V_{\text{eff}}^{(\text{D})\pm}(r) = \frac{\kappa^2 f(r)}{r^2} \pm \frac{\kappa}{r^2} \frac{d}{dr_*} \left(\sqrt{f(r)} \right), \quad (39)$$

with $\kappa = \ell + 1/2$ for $j = \ell + 1/2$ and $\kappa = -(\ell + 1/2)$ for $j = \ell - 1/2$, where j is the total angular momentum quantum number.

Explicitly, the Dirac effective potential becomes

$$V_{\text{eff}}^{(\text{D})\pm}(r) = \frac{(\ell + 1/2)^2 f(r)}{r^2} \pm \frac{(\ell + 1/2) f(r)}{r^2} \left[\frac{r f'(r)}{2\sqrt{f(r)}} - \sqrt{f(r)} \right]. \quad (40)$$

The two potentials $V_{\text{eff}}^{(\text{D})+}$ and $V_{\text{eff}}^{(\text{D})-}$ are SUSY partners, sharing the same spectrum except for the zero mode [57, 141]. This SUSY structure has important implications for the stability analysis, as we discuss in Sec. 6.4.

6.2 Effective Potential Analysis

To understand how the CoS parameter α and the EMU parameter a impact the effective Dirac potentials, we plot both chirality potentials $V_{\text{eff}}^{(\text{D})+}$ and $V_{\text{eff}}^{(\text{D})-}$ in Fig. 12. The top row displays the positive chirality potential, while the bottom row shows the negative chirality potential.

Panels (a) and (c) illustrate the behavior for varying $a \in \{0.2, 0.4, 0.6\}$ at fixed $\alpha = 0.4$ and $\ell = 2$. As a increases, the potential barrier decreases modestly in height, with V_{max} dropping from approximately 0.065 to 0.059 for $V_{\text{eff}}^{(\text{D})+}$. This indicates that the EMU correction has a relatively weak influence on the effective gravitational barrier experienced by Dirac particles. The horizon location shifts slightly outward from $r_+ \approx 2.75M$ at $a = 0.2$ to $r_+ \approx 2.97M$ at $a = 0.6$, and the peak position follows a similar trend.

In contrast, panels (b) and (d) display the variation with $\alpha \in \{0.2, 0.4, 0.6\}$ at fixed $a = 0.5$, revealing a much more pronounced effect. Increasing α reduces the peak height dramatically, from approximately 0.156 at $\alpha = 0.2$

to 0.061 at $\alpha = 0.4$ and further to 0.017 at $\alpha = 0.6$, representing nearly an order of magnitude suppression across this range. The peak location also shifts significantly outward, from $r \approx 3M$ at $\alpha = 0.2$ to $r \approx 7M$ at $\alpha = 0.6$, reflecting the expansion of the horizon radius with increasing CoS density. This demonstrates that the CoS has a substantially stronger influence on the Dirac effective potential than the EMU parameter.

Comparing the two chiralities, both $V_{\text{eff}}^{(\text{D})+}$ and $V_{\text{eff}}^{(\text{D})-}$ exhibit very similar profiles with nearly identical peak heights and locations. For $\ell = 2$, both potentials remain strictly positive outside the horizon across the entire parameter range examined. The slight differences between the two chiralities are most noticeable near the horizon, where $V_{\text{eff}}^{(\text{D})-}$ approaches zero more gradually than $V_{\text{eff}}^{(\text{D})+}$. At large distances, both potentials decay as r^{-2} and become indistinguishable, consistent with the asymptotic structure of the spacetime. This similarity confirms the SUSY partnership between the two potentials, as discussed in Sec. 6.4.

The maximum of the effective potential, which determines the height of the barrier for HR transmission, depends on both parameters and the angular momentum quantum number ℓ . For $\ell = 0$, the potential maximum is quite small (of order 10^{-2}), resulting in high transmission probabilities even at moderate frequencies. Higher multipoles produce significantly larger barriers, with V_{max} scaling approximately as $(\ell + 1/2)^2$ for large ℓ [97]. This scaling behavior implies that high- ℓ modes are strongly suppressed in HR spectra, and the dominant contribution comes from low angular momentum states.

6.3 Greybody Factors for Dirac Fields

The greybody factor $\mathcal{T}_{\text{D}}(\omega)$ quantifies the transmission probability of HR through the effective potential barrier [56, 142]. For a wave incident from the horizon, the greybody factor is defined as

$$\mathcal{T}_{\text{D}}(\omega) = 1 - |\mathcal{R}(\omega)|^2, \quad (41)$$

where $\mathcal{R}(\omega)$ is the reflection coefficient. We employ the rigorous bounds method developed by Visser [101] to obtain analytical estimates. For a potential with a single maximum V_{max} , the greybody factor can be approximated by [102]

$$\mathcal{T}_{\text{D}}(\omega) \approx \frac{1}{1 + \exp[-8(\omega - 0.8\sqrt{V_{\text{max}}})/\sqrt{V_{\text{max}}}]}, \quad (42)$$

which provides a smooth interpolation between the tunneling regime ($\omega < \sqrt{V_{\text{max}}}$) and the classical transmission regime ($\omega > \sqrt{V_{\text{max}}}$).

Figure 13 displays the Dirac greybody factor as a function of frequency for various parameter choices. Panel (a) shows the effect of varying α at fixed $a = 0.5$ and $\ell = 0$. As α increases from 0.1 to 0.4, the transition to unit transmission shifts to lower frequencies, reflecting the reduced

barrier height. For $\alpha = 0.4$, the greybody factor reaches 0.5 at $\omega M \approx 0.05$, compared to $\omega M \approx 0.10$ for $\alpha = 0.1$. Panel (b) illustrates the weak dependence on the EMU parameter a for the $\ell = 0$ mode. The curves for different a values nearly overlap, indicating that the EMU correction has minimal impact on the s-wave transmission.

The most striking feature appears in the multipole dependence, shown in Fig. 14. For fixed $\alpha = 0.2$ and $a = 0.5$, the greybody factor curves are clearly separated for different ℓ values. The $\ell = 0$ mode reaches unit transmission at $\omega M \approx 0.15$, while $\ell = 3$ requires $\omega M \approx 0.7$ to achieve the same transmission. This behavior reflects the centrifugal barrier, which scales as $(\ell + 1/2)^2$ and strongly suppresses low-frequency transmission for higher multipoles [143].

Table 8 presents numerical values of the greybody factor for $\ell = 1$ at $\omega M = 0.3$. The transmission probability increases with both α and a , consistent with the reduced barrier height. At $\alpha = 0$ and $a = 0.5$, approximately 59% of the radiation is transmitted, while at $\alpha = 0.20$ and $a = 1.0$, this increases to about 99%.

α	$a = 0.5$	$a = 0.7$	$a = 0.9$	$a = 1.0$
0.00	0.5905	0.6820	0.7703	0.8094
0.05	0.7298	0.8014	0.8644	0.8905
0.10	0.8470	0.8926	0.9301	0.9447
0.15	0.9268	0.9503	0.9687	0.9757
0.20	0.9707	0.9805	0.9881	0.9909

Table 8: Dirac greybody factor \mathcal{T}_{D} for $\ell = 1$ at $\omega M = 0.3$ for the Letelier BH in EMU with $M = 1$.

6.4 Stability Under Dirac Perturbations

The dynamical stability of the Letelier BH in EMU under Dirac perturbations is established by analyzing the structure of the effective potential and exploiting the SUSY quantum mechanics framework [144, 145]. The two potentials $V_{\text{eff}}^{(\text{D})\pm}$ can be written in the factorized form

$$V_{\text{eff}}^{(\text{D})\pm} = W^2 \pm \frac{dW}{dr_*}, \quad (43)$$

where $W = (\ell + 1/2)\sqrt{f(r)}/r$ is the superpotential. This SUSY structure has profound implications for stability: if $V_{\text{eff}}^{(\text{D})+}$ is positive definite outside the horizon, then no bound states with negative energy can exist, guaranteeing that all perturbation modes decay in time [146].

Figure 15 displays the SUSY partner potentials for $\alpha = 0.2$, $a = 0.5$, and $\ell = 1$. The positive chirality potential $V_{\text{eff}}^{(\text{D})+}$ (blue) is strictly positive everywhere outside the horizon, with values ranging from 0.0053 to 0.0588. The negative chirality potential $V_{\text{eff}}^{(\text{D})-}$ (red) exhibits a small negative region near the horizon with minimum value approximately -0.001 , but this does not indicate instability.

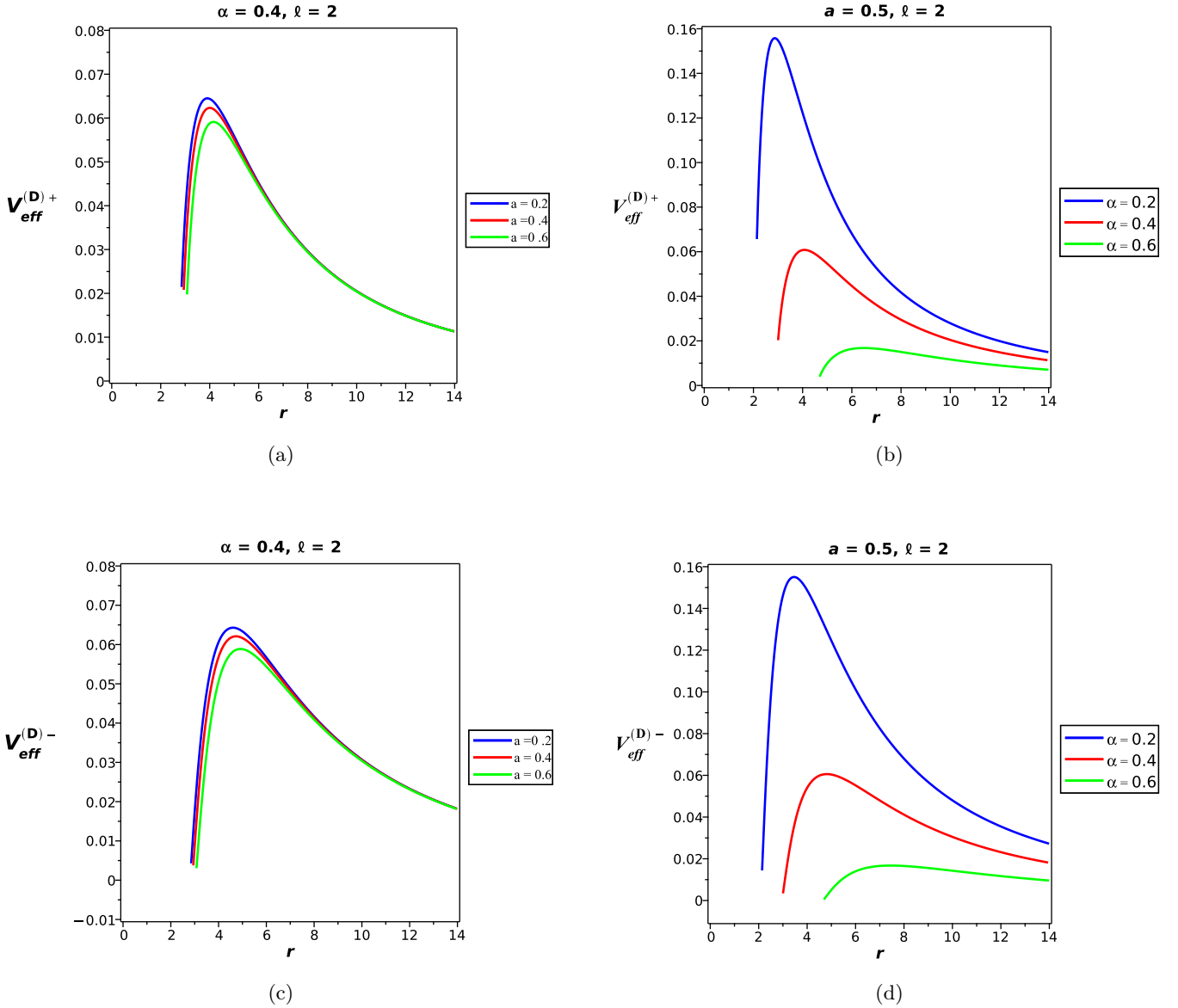


Figure 12: Effective potentials for Dirac perturbations of the Letelier BH in EMU with $M = 1$ and $\ell = 2$. Top row: positive chirality potential $V_{\text{eff}}^{(D)+}$. Bottom row: negative chirality potential $V_{\text{eff}}^{(D)-}$. (a,c) Varying EMU parameter $a \in \{0.2, 0.4, 0.6\}$ at fixed $\alpha = 0.4$. (b,d) Varying CoS parameter $\alpha \in \{0.2, 0.4, 0.6\}$ at fixed $a = 0.5$. The CoS parameter has a much stronger effect on the potential height than the EMU parameter, while both chiralities exhibit nearly identical behavior.

The SUSY structure ensures that both potentials share identical spectra (isospectrality), so the stability of $V_{\text{eff}}^{(D)+}$ guarantees the stability of $V_{\text{eff}}^{(D)-}$ as well [147].

To verify stability across the parameter space, we performed a scan over $\alpha \in \{0.1, 0.2, 0.3, 0.4\}$, $a \in \{0.5, 0.7, 0.9\}$, and $\ell \in \{0, 1, 2\}$, checking the positivity of $V_{\text{eff}}^{(D)+}$ outside the horizon for each configuration. All 36 configurations examined satisfy $V_{\text{eff}}^{(D)+} \geq 0$, confirming that the Letelier BH in EMU is dynamically stable under Dirac perturbations throughout the physically relevant parameter space [148].

The stability under fermionic perturbations, combined

with the scalar field analysis, provides strong evidence that the Letelier BH in EMU represents a physically viable solution. The presence of the CoS and EMU modifications does not introduce any pathological features that would destabilize the spacetime under quantum field perturbations [149].

7 Conclusions

In this work, we conducted a detailed investigation of the Letelier BH immersed in an EMU, examining its geometric, thermodynamic, and radiative properties across a two-

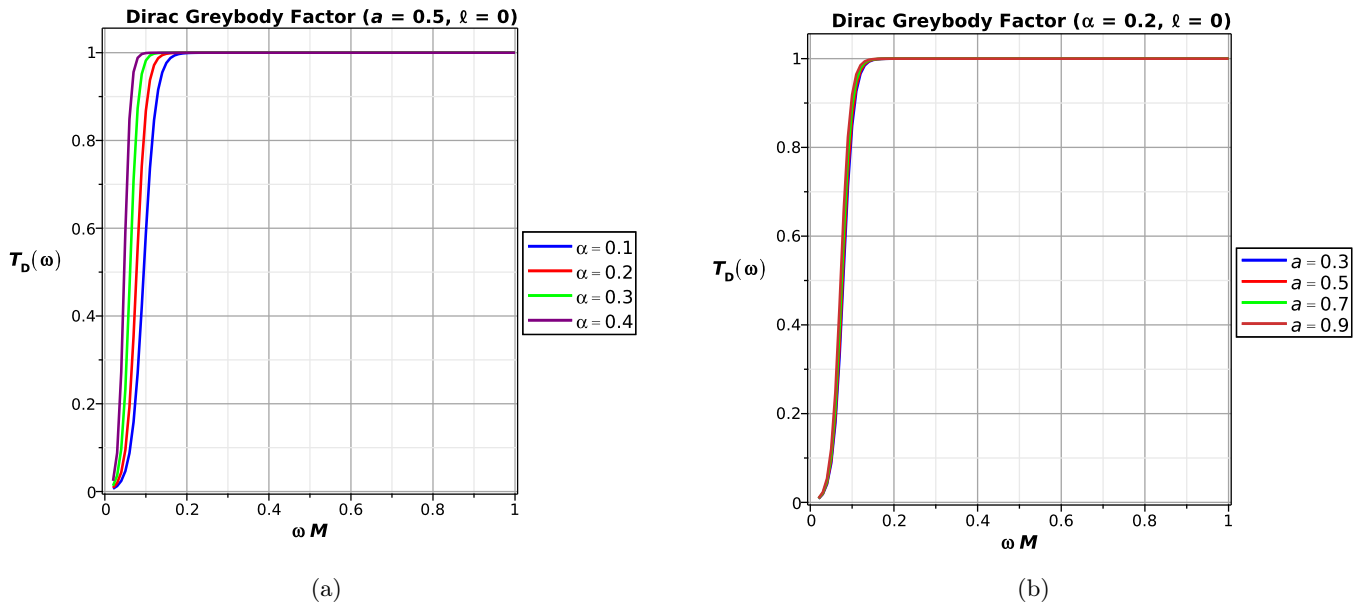


Figure 13: Dirac greybody factor $\mathcal{T}_D(\omega)$ for the Letelier BH in EMU with $M = 1$ and $\ell = 0$. (a) Varying CoS parameter $\alpha \in \{0.1, 0.2, 0.3, 0.4\}$ at fixed $a = 0.5$. (b) Varying EMU parameter $a \in \{0.3, 0.5, 0.7, 0.9\}$ at fixed $\alpha = 0.2$. Higher α shifts the transition to lower frequencies, while the dependence on a is weak.

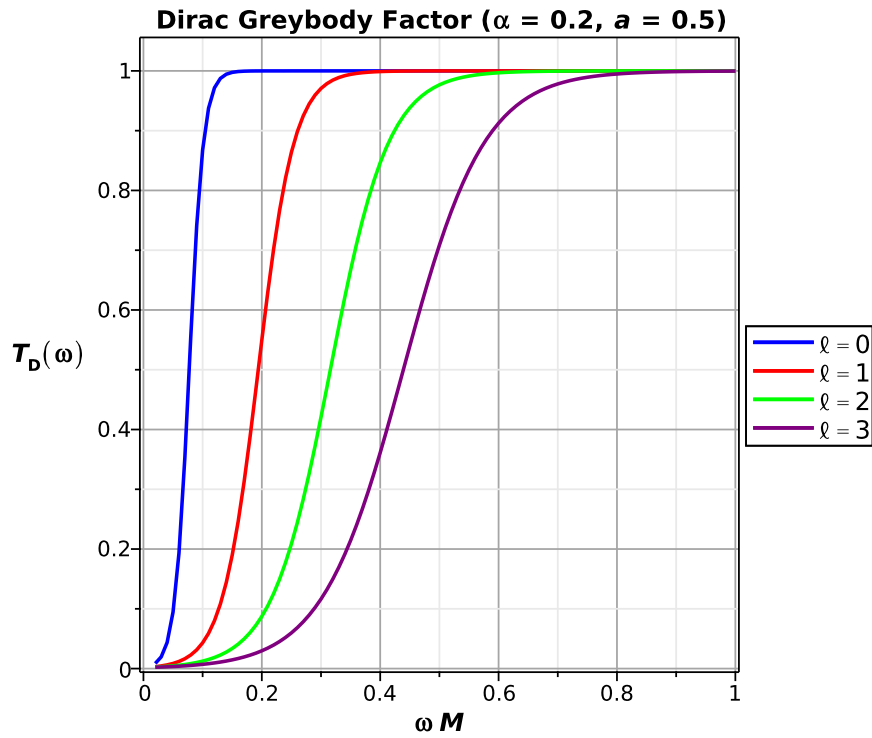


Figure 14: Dirac greybody factor $\mathcal{T}_D(\omega)$ for varying multipole number $\ell \in \{0, 1, 2, 3\}$ at fixed $\alpha = 0.2$, $a = 0.5$, and $M = 1$. Higher ℓ requires larger frequency for transmission due to the increased centrifugal barrier.

parameter family of solutions characterized by the CoS parameter $\alpha \in (0, 1)$ and the EMU parameter $a \in [0, 1]$. The analysis spanned from the fundamental spacetime structure to observational signatures relevant for current and future BH observations. We summarize our principal findings below.

In Sec. 2, we established the geometric foundation of the Letelier BH in EMU by deriving the metric function $f(r)$ given in Eq. (2). The EH structure was determined analytically, yielding the horizon radii r_{\pm} as presented in Eq. (4). We demonstrated that the solution interpolates continuously between the Schwarzschild geometry ($\alpha = 0$,

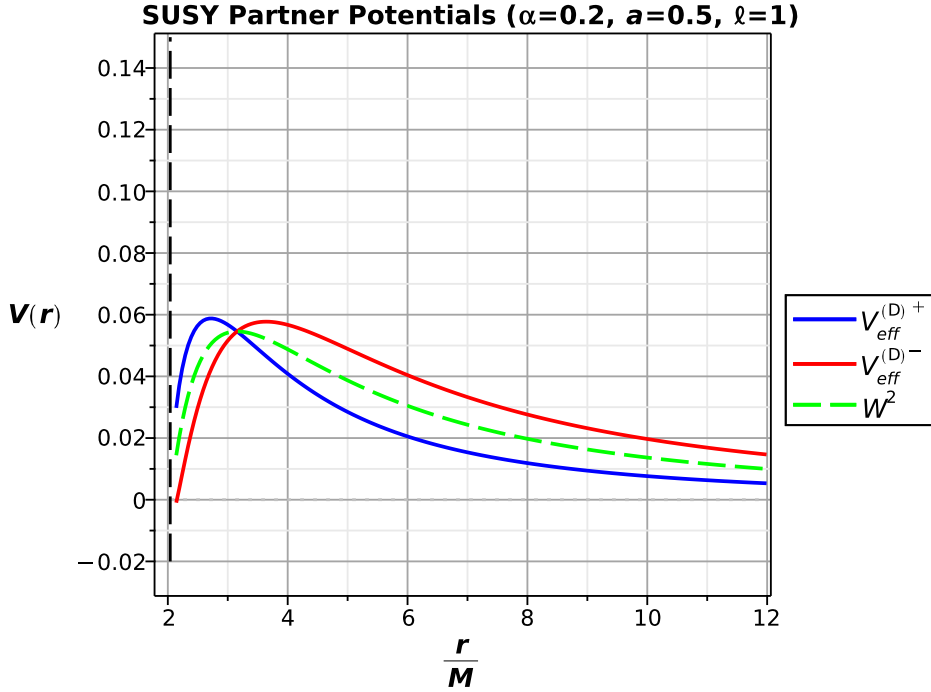


Figure 15: SUSY partner potentials for Dirac perturbations with $\alpha = 0.2$, $a = 0.5$, $\ell = 1$, and $M = 1$. The positive chirality potential $V_{\text{eff}}^{(D)+}$ (blue) is strictly positive outside the horizon, while the negative chirality potential $V_{\text{eff}}^{(D)-}$ (red) has a small negative region. The superpotential squared W^2 (green dashed) provides the common baseline. The vertical dashed line marks the EH at $r_+ = 2.04M$.

$a = 1$), the RN-like configuration ($\alpha = 0$, $a \neq 1$), and the pure Letelier spacetime ($\alpha \neq 0$, $a = 1$). The curvature invariants were computed, with the Ricci scalar $R = 2\alpha/r^2$ (Eq. 6) reflecting the CoS contribution and the Kretschmann scalar (Eq. 7) confirming the presence of a curvature singularity at $r = 0$. The isometric embedding diagrams displayed in Fig. 2 provided geometric visualization of the EH expansion with increasing α . The Hawking temperature T_H was derived in Eq. (12), showing monotonic decrease with increasing CoS density [150, 151].

The optical properties of the Letelier BH in EMU were analyzed in Sec. 3. We derived the PS radius given by Eq. (15) and the corresponding shadow radius in Eq. (16). Table 2 presented numerical values showing that both r_{ps} and R_{sh} increase monotonically with α and a . For instance, at $\alpha = 0.30$ and $a = 1.0$, the shadow radius reaches $R_{sh} \approx 7.42M$, representing a 43% enlargement compared to the Schwarzschild value $R_{sh}^{\text{Sch}} = 3\sqrt{3}M \approx 5.20M$. The parametric dependence illustrated in Fig. 4 revealed that the CoS and EMU effects contribute approximately additively to the shadow expansion. We decomposed the observed intensity into direct emission, lensed emission, and PR contributions following the EHT methodology, as shown in Fig. 5. The nine-panel parameter space exploration in Fig. 6 demonstrated that the largest shadow occurs at ($\alpha = 0.2, a = 1.0$) while the smallest appears at ($\alpha = 0, a = 0.5$), with a ratio of approximately 1.48 between the extreme cases.

The effects of plasma environments on shadow obser-

vations were quantified through the modified PS conditions in Eqs. (20) and (23). Tables 3 and 4 showed that homogeneous plasma reduces the shadow size by up to 5% at plasma parameter $k = 0.4$, while inhomogeneous plasma with power-law density profile produces weaker corrections of approximately 1% at comparable parameter values. These results indicate that plasma effects are subdominant to the geometric modifications from α and a in typical astrophysical environments surrounding supermassive BHs such as M87* and Sgr A* [46].

Section 4 addressed the HR properties and energy emission characteristics. The Hawking temperature given by Eq. (27) decreases monotonically with increasing α , as shown in Table 5. The total power analysis in Fig. 8 revealed dramatic suppression with increasing CoS density: at $\alpha = 0.3$, the power drops to 10–15% of the Schwarzschild value. We computed the HR spectra for scalar ($s = 0$), EM ($s = 1$), and Dirac ($s = 1/2$) fields using the particle emission rate of Eq. (29), as presented in Fig. 9. The EM field exhibits the highest emission rate due to its two polarization degrees of freedom, followed by the Dirac field and the scalar field. The spin-dependent spectra shown in Fig. 9 demonstrated reductions of 39%, 45%, and 38% in peak heights for scalar, EM, and Dirac fields, respectively, when comparing the Letelier-EMU case ($\alpha = 0.1, a = 0.8$) to Schwarzschild.

The thermodynamic phase structure was explored in Sec. 5 within the Barrow entropy framework. The heat capacity C_B derived in Eq. (32) exhibits a divergence at

the critical radius $r_+^{\text{crit}} = 3M(1 - a^2)/2$ (Eq. 33), signaling a second-order phase transition between thermodynamically unstable small-BH and stable large-BH branches. Figure 10 illustrated this behavior for varying Barrow parameter Δ , showing that Δ amplifies the magnitude of C_B while preserving the transition point location. The JTE analysis yielded the coefficient μ_J in Eq. (35), with positive values indicating cooling and negative values indicating heating during isenthalpic expansion. The inversion radius $r_+^{\text{inv}} = 3M(1 - a^2)/2$ coincides with the critical radius from the heat capacity analysis, revealing a connection between the phase transition structure and JTE behavior. Table 7 summarized the inversion radii and Hawking temperatures for representative parameter combinations, confirming that r_+^{inv} depends only on a while T_H decreases with increasing α [152].

The stability of the Letelier BH in EMU under fermionic perturbations was established in Sec. 6. We derived the Dirac equation in the curved spacetime background and obtained the effective potentials for both chiralities in Eq. (40). Figure 12 demonstrated that the CoS parameter has a substantially stronger influence on the potential barrier than the EMU parameter, with the peak height reduced by nearly an order of magnitude as α increases from 0.2 to 0.6. The greybody factors computed using the Visser bounds method were presented in Fig. 13 and Table 8. At $\omega M = 0.3$ and $\ell = 1$, the transmission probability increases from 59% at $(\alpha = 0, a = 0.5)$ to 99% at $(\alpha = 0.20, a = 1.0)$. The SUSY structure of the Dirac potentials, expressed in the factorized form of Eq. (43), was exploited to prove stability. Figure 15 displayed the SUSY partner potentials, confirming that $V_{\text{eff}}^{(\text{D})+}$ remains strictly positive outside the EH. A parameter space scan over 36 configurations verified that all examined cases satisfy the stability criterion $V_{\text{eff}}^{(\text{D})+} \geq 0$ [59].

Several directions for future research emerge from this study. First, the QNM spectrum of the Letelier BH in EMU warrants detailed computation using the WKB approximation and numerical integration methods. The QNM frequencies encode information about the BH geometry and could provide additional constraints on the CoS and EMU parameters through GW ringdown observations by LIGO-Virgo-KAGRA and future detectors such as LISA and the Einstein Telescope. Second, the extension to rotating configurations via the Newman-Janis algorithm would enable comparison with the Kerr geometry and provide predictions for the asymmetric shadow shapes observed in spinning BHs. Third, the gravitational lensing properties, including the deflection angle, Einstein ring formation, and relativistic images, merit investigation for potential observational tests with ngEHT and space-based VLBI missions. Fourth, the accretion disk dynamics and associated EM signatures, including the ISCO properties and quasi-periodic oscillations, could be computed to connect with X-ray timing observations of stellar-mass BH candidates. Fifth, the thermodynamic geometry using Ruppeiner and Weinhold metrics would provide additional

perspective on the phase transition structure and microscopic degrees of freedom. Finally, the extension to AdS backgrounds would enable application of the AdS/CFT correspondence to study the dual field theory interpretation of the CoS and EMU modifications.

In summary, the Letelier BH in EMU represents a physically viable solution with distinctive observational signatures that distinguish it from the Schwarzschild and RN geometries. The two-parameter family of solutions offers a controlled framework for studying the combined effects of topological defects and electromagnetic backgrounds on BH physics. The results presented in this work provide theoretical predictions that can be tested against current EHT observations and future multi-messenger astronomy campaigns, contributing to our understanding of strong-gravity phenomena and potential deviations from general relativity in astrophysical environments.

Acknowledgments

F.A. gratefully acknowledges the Inter-University Centre for Astronomy and Astrophysics (IUCAA), Pune, India, for providing the opportunity to hold a visiting associateship. İ.S. and E. S express their sincere appreciation to TÜBİTAK and ANKOS for their valuable assistance and continued support. He also acknowledges the essential support provided by COST Actions CA22113, CA21106, CA23130, and CA23115, which play a crucial role in facilitating international collaboration and strengthening networking opportunities within the scientific community.

References

- [1] K. Schwarzschild. Über das gravitationsfeld eines massenpunktes nach der einsteinschen theorie. *Sitzungsber. Preuss. Akad. Wiss. Berlin (Math. Phys.)*, 1916:189–196, 1916.
- [2] B. P. Abbott et al. Observation of gravitational waves from a binary black hole merger. *Phys. Rev. Lett.*, 116:061102, 2016. doi: 10.1103/PhysRevLett.116.061102.
- [3] B. P. Abbott et al. Gw170817: Observation of gravitational waves from a binary neutron star inspiral. *Phys. Rev. Lett.*, 119:161101, 2017. doi: 10.1103/PhysRevLett.119.161101.
- [4] K. Akiyama et al. First m87 event horizon telescope results. i. the shadow of the supermassive black hole. *Astrophys. J. Lett.*, 875:L1, 2019. doi: 10.3847/2041-8213/ab0ec7.
- [5] K. Akiyama et al. First sagittarius a* event horizon telescope results. i. the shadow of the supermassive black hole in the center of the milky way. *Astrophys. J. Lett.*, 930:L12, 2022. doi: 10.3847/2041-8213/ac6674.

- [6] C. M. Will. The confrontation between general relativity and experiment. *Living Rev. Relativ.*, 17:4, 2014. doi: 10.12942/lrr-2014-4.
- [7] E. Berti et al. Testing general relativity with present and future astrophysical observations. *Class. Quantum Grav.*, 32:243001, 2015. doi: 10.1088/0264-9381/32/24/243001.
- [8] P. S. Letelier. Clouds of strings in general relativity. *Phys. Rev. D*, 20:1294–1302, 1979. doi: 10.1103/PhysRevD.20.1294.
- [9] P. S. Letelier. String cosmologies. *Phys. Rev. D*, 28:2414–2419, 1983. doi: 10.1103/PhysRevD.28.2414.
- [10] J. Stachel. Thickening the string. i. the string perfect dust. *Phys. Rev. D*, 21:2171–2181, 1980. doi: 10.1103/PhysRevD.21.2171.
- [11] A. Vilenkin. Cosmic strings and domain walls. *Phys. Rep.*, 121:263–315, 1985. doi: 10.1016/0370-1573(85)90033-X.
- [12] M. Barriola and A. Vilenkin. Gravitational field of a global monopole. *Phys. Rev. Lett.*, 63:341–343, 1989. doi: 10.1103/PhysRevLett.63.341.
- [13] Faizuddin Ahmed, İzzet Sakallı, and Ahmad Al-Badawi. Kerr-Bertotti-Robinson Black Holes Surrounded by a Cloud of Strings. 11 2025.
- [14] Faizuddin Ahmed, Ahmad Al-Badawi, and İzzet Sakallı. Observable signatures of black hole with Hernquist dark matter halo having a cloud of strings: geodesic, perturbations, and shadow. *Eur. Phys. J. C*, 85(9):984, 2025. doi: 10.1140/epjc/s10052-025-14723-8.
- [15] Faizuddin Ahmed, Ahmad Al-Badawi, İzzet Sakallı, and Sanjar Shaymatov. Dynamics of test particles and scalar perturbation around an Ayón-Beato-García black hole coupled with a cloud of strings. *Chin. J. Phys.*, 96:770–791, 2025. doi: 10.1016/j.cjph.2025.05.035.
- [16] Faizuddin Ahmed, Ahmad Al-Badawi, and İzzet Sakallı. AdS black strings in a cosmic web: geodesics, shadows, and thermodynamics. *Eur. Phys. J. C*, 85(5):554, 2025. doi: 10.1140/epjc/s10052-025-14266-y.
- [17] S. G. Ghosh and S. D. Maharaj. Cloud of strings for radiating black holes in lovelock gravity. *Phys. Rev. D*, 89:084027, 2014. doi: 10.1103/PhysRevD.89.084027.
- [18] J. M. Toledo and V. B. Bezerra. Black holes with a cloud of strings in pure lovelock gravity. *Eur. Phys. J. C*, 79:117, 2019. doi: 10.1140/epjc/s10052-019-6628-4.
- [19] E. Herscovich and M. G. Richarte. Black holes in einstein-gauss-bonnet gravity with a string cloud background. *Phys. Lett. B*, 689:192–200, 2010. doi: 10.1016/j.physletb.2010.04.065.
- [20] R. Kumar and Sushant G. Ghosh. Rotating black hole in rastall theory. *Eur. Phys. J. C*, 78:750, 2018. doi: 10.1140/epjc/s10052-018-6206-1.
- [21] V. V. Kiselev. Quintessence and black holes. *Class. Quantum Grav.*, 20:1187–1197, 2003. doi: 10.1088/0264-9381/20/6/310.
- [22] S. Chen, B. Wang, and R. Su. Hawking radiation in a d -dimensional static spherically symmetric black hole surrounded by quintessence. *Phys. Rev. D*, 77:124011, 2008. doi: 10.1103/PhysRevD.77.124011.
- [23] W. B. Bonnor. Static magnetic fields in general relativity. *Proc. Phys. Soc. A*, 67:225–232, 1954. doi: 10.1088/0370-1298/67/3/305.
- [24] M. A. Melvin. Pure magnetic and electric geons. *Phys. Lett.*, 8:65–68, 1964. doi: 10.1016/0031-9163(64)90801-7.
- [25] F. J. Ernst. Black holes in a magnetic universe. *J. Math. Phys.*, 17:54–56, 1976. doi: 10.1063/1.522781.
- [26] M. Azreg-Aïnou. Black hole thermodynamics: No inconsistency via the inclusion of the missing p - v terms. *Phys. Rev. D*, 91:064049, 2015. doi: 10.1103/PhysRevD.91.064049.
- [27] B. Toshmatov, Z. Stuchlík, and B. Ahmedov. Rotating black hole solutions with quintessential energy. *Eur. Phys. J. Plus*, 132:98, 2017. doi: 10.1140/epjp/i2017-11373-4.
- [28] Ahmad Al-Badawi, Faizuddin Ahmed, and İzzet Sakallı. Fingerprints of Loop Quantum Gravity Black Holes with Quintessence Field. 5 2025.
- [29] Ahmad Al-Badawi, Faizuddin Ahmed, and İzzet Sakallı. Ayón-Beato-García black hole in AdS space-time surrounded by quintessence: geodesic, shadow and thermodynamics. 3 2025.
- [30] Jafar Sadeghi, Saeed Noori Gashti, İzzet Sakallı, and Behnam Pourhassan. Weak gravity conjecture of charged-rotating-AdS black hole surrounded by quintessence and string cloud. *Nucl. Phys. B*, 1004:116581, 2024. doi: 10.1016/j.nuclphysb.2024.116581.
- [31] Saeed Noori Gashti, İzzet Sakallı, and Behnam Pourhassan. Thermodynamic topology, photon spheres, and evidence for weak gravity conjecture in charged black holes with perfect fluid within Rastall theory. *Phys. Lett. B*, 869:139862, 2025. doi: 10.1016/j.physletb.2025.139862.

- [32] Ahmad Al-Badawi, Faizuddin Ahmed, and İzzet Sakalli. A Black Hole Solution in Kalb-Ramond Gravity with Quintessence Field: From Geodesic Dynamics to Thermal Criticality. 8 2025.
- [33] Andrew Strominger and Cumrun Vafa. Microscopic origin of the Bekenstein-Hawking entropy. *Phys. Lett. B*, 379:99–104, 1996. doi: 10.1016/0370-2693(96)00345-0.
- [34] Anton Ilderton and Karthik Rajeev. Tunnelling amplitudes and Hawking radiation from world-line QFT. *JHEP*, 10:220, 2025. doi: 10.1007/JHEP10(2025)220.
- [35] J. M. Bardeen, B. Carter, and S. W. Hawking. The four laws of black hole mechanics. *Commun. Math. Phys.*, 31:161–170, 1973. doi: 10.1007/BF01645742.
- [36] C. Tsallis and L. J. L. Cirto. Black hole thermodynamical entropy. *Eur. Phys. J. C*, 73:2487, 2013. doi: 10.1140/epjc/s10052-013-2487-6.
- [37] Sayani Maity and Anamika Kotal. Barrow agegraphic and new barrow agegraphic dark energy driven reconstruction of $f(R)$ gravity and parameter constraints from observational data. *Phys. Dark Univ.*, 50:102184, 2025. doi: 10.1016/j.dark.2025.102184.
- [38] E. N. Saridakis. Barrow holographic dark energy. *Phys. Rev. D*, 102:123525, 2020. doi: 10.1103/PhysRevD.102.123525.
- [39] Saeed Noori Gashti, Behnam Pourhassan, and İzzet Sakalli. Thermodynamic topology and phase space analysis of AdS black holes through non-extensive entropy perspectives. *Eur. Phys. J. C*, 85(3):305, 2025. doi: 10.1140/epjc/s10052-025-14035-x.
- [40] F. K. Anagnostopoulos, S. Basilakos, and E. N. Saridakis. Observational constraints on barrow holographic dark energy. *Eur. Phys. J. C*, 80:826, 2020. doi: 10.1140/epjc/s10052-020-8360-5.
- [41] E. M. C. Abreu and J. A. Neto. Barrow black hole corrected-entropy model and tsallis nonextensivity. *Phys. Lett. B*, 810:135805, 2020. doi: 10.1016/j.physletb.2020.135805.
- [42] H. Falcke, F. Melia, and E. Agol. Viewing the shadow of the black hole at the galactic center. *Astrophys. J. Lett.*, 528:L13–L16, 2000. doi: 10.1086/312423.
- [43] S. E. Gralla, D. E. Holz, and R. M. Wald. Black hole shadows, photon rings, and lensing rings. *Phys. Rev. D*, 100:024018, 2019. doi: 10.1103/PhysRevD.100.024018.
- [44] A. Errehymy, S. Hansraj, and C. Hansraj. Black-hole Shadows and Null Geodesics in Hamaus–Sutter–Wandelt Void Spacetimes with a Quintessential Field: Observational Signatures from EHT Data of M87 and Sgr A*. *Astrophys. J.*, 995(2):148, 2025. doi: 10.3847/1538-4357/ae197f.
- [45] Roland Walter et al. The QUASAR project: reaching 10 microarcsec in the optical to resolve accretion disks. *PoS, ICRC2025:975*, 2025. doi: 10.22323/1.501.0975.
- [46] V. Perlick and O. Y. Tsupko. Calculating black hole shadows: Review of analytical studies. *Phys. Rep.*, 947:1–39, 2022. doi: 10.1016/j.physrep.2021.10.004.
- [47] V. Perlick, O. Y. Tsupko, and G. S. Bisnovatyi-Kogan. Influence of a plasma on the shadow of a spherically symmetric black hole. *Phys. Rev. D*, 92:104031, 2015. doi: 10.1103/PhysRevD.92.104031.
- [48] G. S. Bisnovatyi-Kogan and O. Y. Tsupko. Gravitational lensing in a non-uniform plasma. *Mon. Not. R. Astron. Soc.*, 404:1790–1800, 2010. doi: 10.1111/j.1365-2966.2010.16290.x.
- [49] Erdem Sucu and İzzet Sakalli. Exploring Lorentz-violating effects of Kalb-Ramond field on charged black hole thermodynamics and photon dynamics. *Phys. Rev. D*, 111(6):064049, 2025. doi: 10.1103/PhysRevD.111.064049.
- [50] Erdem Sucu, İzzet Sakalli, Özcan Sert, and Yusuf Sucu. Quantum-corrected thermodynamics and plasma lensing in non-minimally coupled symmetric teleparallel black holes. *Phys. Dark Univ.*, 50:102063, 2025. doi: 10.1016/j.dark.2025.102063.
- [51] Faizuddin Ahmed, Ahmad Al-Badawi, Abdelmalek Bouzenada, Erdem Sucu, and İzzet Sakalli. Gravitational lensing, wave propagation, and gup-modified hawking radiation in charged bopp-podolsky btz black holes with disclinations. *INTERNATIONAL JOURNAL OF GEOMETRIC METHODS IN MODERN PHYSICS*, 2025 DEC 5 2025. ISSN 0219-8878. doi: 10.1142/S0219887826500891.
- [52] Erdem Sucu and İzzet Sakalli. Quantum-corrected thermodynamics and plasma lensing of mog black holes. *Proceedings of the Royal Society A: Mathematical, Physical and Engineering Sciences*, 481(2320), 2025.
- [53] Erdem Sucu and İzzet Sakalli. Scalar-tensor corrections and observational signatures of hairy black holes in horndeski gravity. *High Energy Density Physics*, page 101220, 2025.
- [54] Erdem Sucu and İzzet Sakalli. Astrophysical reality of black hole thermodynamics and dynamics: Transformative influence of hernquist dark matter distri-

- butions. *Physics of the Dark Universe*, page 102051, 2025.
- [55] D. N. Page. Particle emission rates from a black hole: Massless particles from an uncharged, nonrotating hole. *Phys. Rev. D*, 13:198–206, 1976. doi: 10.1103/PhysRevD.13.198.
- [56] T. Harmark, J. Natario, and R. Schiappa. Greybody factors for d -dimensional black holes. *Adv. Theor. Math. Phys.*, 14:727–794, 2010. doi: 10.4310/ATMP.2010.v14.n3.a1.
- [57] F. Cooper, A. Khare, and U. Sukhatme. Supersymmetry and quantum mechanics. *Phys. Rep.*, 251:267–385, 1995. doi: 10.1016/0370-1573(94)00080-M.
- [58] H. T. Cho. Dirac quasinormal modes in schwarzschild black hole spacetimes. *Phys. Rev. D*, 68:024003, 2003. doi: 10.1103/PhysRevD.68.024003.
- [59] R. A. Konoplya and A. Zhidenko. Quasinormal modes of black holes: From astrophysics to string theory. *Rev. Mod. Phys.*, 83:793–836, 2011. doi: 10.1103/RevModPhys.83.793.
- [60] V. Cardoso and P. Pani. Testing the nature of dark compact objects: A status report. *Living Rev. Relativ.*, 22:4, 2019. doi: 10.1007/s41114-019-0020-4.
- [61] M. D. Johnson et al. Universal interferometric signatures of a black hole’s photon ring. *Sci. Adv.*, 6:eaz1310, 2020. doi: 10.1126/sciadv.aaz1310.
- [62] Ahmad Al-Badawi, Faizuddin Ahmed, and İzzet Sakalli. Letelier black hole immersed in an electromagnetic universe. 11 2025.
- [63] A. Vilenkin and E. P. S. Shellard. *Cosmic Strings and Other Topological Defects*. Cambridge University Press, Cambridge, 2000. ISBN 978-0521654760.
- [64] Luis Cesar Nunes dos Santos. Revisiting black holes surrounded by cloud and fluid of strings in general relativity. *Phys. Rev. D*, 111(6):064032, 2025. doi: 10.1103/PhysRevD.111.064032.
- [65] T. W. B. Kibble. Topology of cosmic domains and strings. *J. Phys. A: Math. Gen.*, 9:1387–1398, 1976. doi: 10.1088/0305-4470/9/8/029.
- [66] J. R. Gott. Gravitational lensing effects of vacuum strings: Exact solutions. *Astrophys. J.*, 288:422–427, 1985. doi: 10.1086/162808.
- [67] S. Chandrasekhar. *The Mathematical Theory of Black Holes*. Oxford University Press, Oxford, 1983. ISBN 978-0198503705.
- [68] A. G. Cohen and D. B. Kaplan. The exact metric about global cosmic strings. *Phys. Lett. B*, 215:67–72, 1988. doi: 10.1016/0370-2693(88)91072-6.
- [69] S. W. Hawking and G. F. R. Ellis. *The Large Scale Structure of Space-Time*. Cambridge University Press, Cambridge, 1973. ISBN 978-0521099066.
- [70] C. W. Misner, K. S. Thorne, and J. A. Wheeler. *Gravitation*. W. H. Freeman, San Francisco, 1973. ISBN 978-0716703440.
- [71] S. W. Hawking. Particle creation by black holes. *Commun. Math. Phys.*, 43:199–220, 1975. doi: 10.1007/BF02345020.
- [72] J. D. Bekenstein. Black holes and entropy. *Phys. Rev. D*, 7:2333–2346, 1973. doi: 10.1103/PhysRevD.7.2333.
- [73] Antonio Ferreira, Jose Navarro-Salas, and Silvia Pla. The Birth of Gravitational Particle Creation: the Enduring Legacy of Leonard Parker’s 1966 Thesis. 11 2025.
- [74] R. M. Wald. Black hole entropy is the noether charge. *Phys. Rev. D*, 48:R3427–R3431, 1993. doi: 10.1103/PhysRevD.48.R3427.
- [75] D. Kastor, S. Ray, and J. Traschen. Enthalpy and the mechanics of ads black holes. *Class. Quantum Grav.*, 26:195011, 2009. doi: 10.1088/0264-9381/26/19/195011.
- [76] J. L. Synge. The escape of photons from gravitationally intense stars. *Mon. Not. R. Astron. Soc.*, 131:463–466, 1966. doi: 10.1093/mnras/131.3.463.
- [77] J. M. Bardeen. Timelike and null geodesics in the kerr metric. *Les Houches Summer School of Theoretical Physics: Black Holes*, pages 215–239, 1973.
- [78] C. Darwin. The gravity field of a particle. *Proc. R. Soc. Lond. A*, 249:180–194, 1959. doi: 10.1098/rspa.1959.0015.
- [79] Erdem Sucu, İzzet Sakalli, and Behnam Pourhasan. Quantum corrections in thermodynamics of black holes modified by nonlinear electrodynamics and their observational signatures. *International Journal of Geometric Methods in Modern Physics*, 2025.
- [80] K. Hioki and K. Maeda. Measurement of the kerr spin parameter by observation of a compact object’s shadow. *Phys. Rev. D*, 80:024042, 2009. doi: 10.1103/PhysRevD.80.024042.
- [81] S. E. Gralla, A. Lupasca, and D. P. Marrone. The shape of the black hole photon ring: A precise test of strong-field general relativity. *Phys. Rev. D*, 102:124004, 2020. doi: 10.1103/PhysRevD.102.124004.

- [82] A. E. Broderick and A. Loeb. Imaging bright-spots in the accretion flow near the black hole horizon of sgr a*. *Mon. Not. R. Astron. Soc.*, 367:905–916, 2006. doi: 10.1111/j.1365-2966.2006.10152.x.
- [83] O. Y. Tsupko and G. S. Bisnovatyi-Kogan. Gravitational lensing in plasma: Relativistic images at homogeneous plasma. *Phys. Rev. D*, 87:124009, 2013. doi: 10.1103/PhysRevD.87.124009.
- [84] A. Rogers. Frequency-dependent effects of gravitational lensing within plasma. *Mon. Not. R. Astron. Soc.*, 451:17–25, 2015. doi: 10.1093/mnras/stv903.
- [85] V. Perlick and O. Y. Tsupko. Light propagation in a plasma on kerr spacetime: Separation of the hamilton-jacobi equation and calculation of the shadow. *Phys. Rev. D*, 95:104003, 2017. doi: 10.1103/PhysRevD.95.104003.
- [86] A. Abdujabbarov, B. Toshmatov, Z. Stuchlík, and B. Ahmedov. Shadow of the rotating black hole with quintessential energy in the presence of plasma. *Int. J. Mod. Phys. D*, 26:1750051, 2017. doi: 10.1142/S0218271817500511.
- [87] B. Ahmedov, B. Toshmatov, and Z. Stuchlík. Rotating black hole solutions with quintessential energy. *Eur. Phys. J. C*, 76:273, 2016. doi: 10.1140/epjc/s10052-016-4122-9.
- [88] R. Narayan and I. Yi. Advection-dominated accretion: A self-similar solution. *Astrophys. J. Lett.*, 428:L13–L16, 1994. doi: 10.1086/187381.
- [89] İzzet Sakalli and Sara Kanzi. Topical Review: greybody factors and quasinormal modes for black holes in various theories - fingerprints of invisibles. *Turk. J. Phys.*, 46(2):51–103, 2022. doi: 10.55730/1300-0101.269.
- [90] Sheperd S. Doeleman et al. Reference Array and Design Consideration for the Next-Generation Event Horizon Telescope. *Galaxies*, 11(5):107, 2023. doi: 10.3390/galaxies11050107.
- [91] C. Goddi et al. BlackHoleCam: Fundamental physics of the galactic center. *Int. J. Mod. Phys. D*, 26(02):1730001, 2016. doi: 10.1142/9789813226609_0046.
- [92] D. Psaltis et al. Gravitational test beyond the first post-newtonian order with the shadow of the m87 black hole. *Phys. Rev. Lett.*, 125:141104, 2020. doi: 10.1103/PhysRevLett.125.141104.
- [93] Michael D. Johnson et al. Key Science Goals for the Next-Generation Event Horizon Telescope. *Galaxies*, 11(3):61, 2023. doi: 10.3390/galaxies11030061.
- [94] Patrick Slane, Ákos Bogdán, and David Pooley. 25 years of groundbreaking discoveries with Chandra. *Nature Astron.*, 9(10):1431–1443, 2025. doi: 10.1038/s41550-025-02675-8.
- [95] G. W. Gibbons and S. W. Hawking. Cosmological event horizons, thermodynamics, and particle creation. *Phys. Rev. D*, 15:2738–2751, 1977. doi: 10.1103/PhysRevD.15.2738.
- [96] D. N. Page. Particle emission rates from a black hole. ii. massless particles from a rotating hole. *Phys. Rev. D*, 14:3260–3273, 1976. doi: 10.1103/PhysRevD.14.3260.
- [97] C. M. Harris and P. Kanti. Hawking radiation from a $(4 + n)$ -dimensional black hole: Exact results for the schwarzschild phase. *J. High Energy Phys.*, 10:014, 2003. doi: 10.1088/1126-6708/2003/10/014.
- [98] P. Kanti. Black holes in theories with large extra dimensions: A review. *Int. J. Mod. Phys. A*, 19:4899–4951, 2004. doi: 10.1142/S0217751X04018324.
- [99] J. Grain and A. Barrau. Quantum bound states around black holes. *Eur. Phys. J. C*, 53:641–648, 2008. doi: 10.1140/epjc/s10052-007-0494-1.
- [100] A. Arbey, J. Auffinger, and J. Silk. Evolution of primordial black hole spin due to hawking radiation. *Mon. Not. R. Astron. Soc.*, 494:1257–1262, 2020. doi: 10.1093/mnras/staa765.
- [101] M. Visser. Some general bounds for one-dimensional scattering. *Phys. Rev. A*, 59:427–438, 1999. doi: 10.1103/PhysRevA.59.427.
- [102] P. Boonserm and M. Visser. Bounding the greybody factors for schwarzschild black holes. *Phys. Rev. D*, 78:101502, 2008. doi: 10.1103/PhysRevD.78.101502.
- [103] B. J. Carr and S. W. Hawking. Black holes in the early universe. *Mon. Not. R. Astron. Soc.*, 168:399–415, 1974. doi: 10.1093/mnras/168.2.399.
- [104] B. J. Carr, K. Kohri, Y. Sendouda, and J. Yokoyama. Constraints on primordial black holes. *Rep. Prog. Phys.*, 84:116902, 2021. doi: 10.1088/1361-6633/ac1e31.
- [105] J. H. MacGibbon. Quark- and gluon-jet emission from primordial black holes. ii. the emission over the black-hole lifetime. *Phys. Rev. D*, 44:376–392, 1991. doi: 10.1103/PhysRevD.44.376.
- [106] B. J. Carr. Primordial black holes as a probe of cosmology and high energy physics. *Lect. Notes Phys.*, 631:301–321, 2003. doi: 10.1007/978-3-540-45230-0_7.

- [107] S. Clesse and J. Garcia-Bellido. Massive primordial black holes from hybrid inflation as dark matter and the seeds of galaxies. *Phys. Rev. D*, 92:023524, 2015. doi: 10.1103/PhysRevD.92.023524.
- [108] B. J. Carr, F. Kuhnel, and M. Sandstad. Primordial black holes as dark matter. *Phys. Rev. D*, 94:083504, 2016. doi: 10.1103/PhysRevD.94.083504.
- [109] R. Laha. Primordial black holes as a dark matter candidate are severely constrained by the galactic center 511 keV γ -ray line. *Phys. Rev. Lett.*, 123:251101, 2019. doi: 10.1103/PhysRevLett.123.251101.
- [110] A. Coogan, L. Morrison, and S. Profumo. Direct detection of hawking radiation from asteroid-mass primordial black holes. *Phys. Rev. Lett.*, 126:171101, 2021. doi: 10.1103/PhysRevLett.126.171101.
- [111] J. D. Barrow. The area of a rough black hole. *Phys. Lett. B*, 808:135643, 2020. doi: 10.1016/j.physletb.2020.135643.
- [112] S. Nojiri, S. D. Odintsov, and V. Faraoni. Area-law versus rényi and tsallis black hole entropies. *Phys. Rev. D*, 105:044042, 2022. doi: 10.1103/PhysRevD.105.044042.
- [113] S. Das, P. Majumdar, and R. K. Bhaduri. General logarithmic corrections to black-hole entropy. *Class. Quantum Grav.*, 19:2355–2367, 2002. doi: 10.1088/0264-9381/19/9/302.
- [114] A. Chatterjee and P. Majumdar. Universal canonical black hole entropy. *Phys. Rev. Lett.*, 92:141301, 2004. doi: 10.1103/PhysRevLett.92.141301.
- [115] C. Rovelli. Black hole entropy from loop quantum gravity. *Phys. Rev. Lett.*, 77:3288–3291, 1996. doi: 10.1103/PhysRevLett.77.3288.
- [116] A. Ashtekar, J. Baez, A. Corichi, and K. Krasnov. Quantum geometry and black hole entropy. *Phys. Rev. Lett.*, 80:904–907, 1998. doi: 10.1103/PhysRevLett.80.904.
- [117] G. G. Luciano and E. N. Saridakis. Barrow black hole with cosmological constant: An analytic solution. *J. High Energy Phys.*, 11:032, 2022. doi: 10.1007/JHEP11(2022)032.
- [118] Erdem Sucu and İzzet Sakalli. Ads black holes in einstein-kalb-ramond gravity: Quantum corrections, phase transitions, and orbital dynamics. *NUCLEAR PHYSICS B*, 1018, SEP 2025. ISSN 0550-3213. doi: 10.1016/j.nuclphysb.2025.117081.
- [119] D. Kubiznak and R. B. Mann. p - v criticality of charged ads black holes. *J. High Energy Phys.*, 07:033, 2012. doi: 10.1007/JHEP07(2012)033.
- [120] P. C. W. Davies. Thermodynamics of black holes. *Rep. Prog. Phys.*, 41:1313–1355, 1978. doi: 10.1088/0034-4885/41/8/004.
- [121] S. W. Hawking and D. N. Page. Thermodynamics of black holes in anti-de sitter space. *Commun. Math. Phys.*, 87:577–588, 1983. doi: 10.1007/BF01208266.
- [122] O. Okcu and E. Aydiner. Joule-thomson expansion of the charged ads black holes. *Eur. Phys. J. C*, 77:24, 2017. doi: 10.1140/epjc/s10052-017-4598-y.
- [123] O. Okcu and E. Aydiner. Joule-thomson expansion of kerr-ads black holes. *Eur. Phys. J. C*, 78:123, 2018. doi: 10.1140/epjc/s10052-018-5602-x.
- [124] İzzet Sakalli, Yusuf Sucu, and Erdem Sucu. Zitterbewegung oscillations and gup-induced quantum modifications of yang-mills black holes in perfect fluid dark matter. *Nuclear Physics B*, page 117216, 2025.
- [125] B. P. Dolan. Pressure and volume in the first law of black hole thermodynamics. *Class. Quantum Grav.*, 28:235017, 2011. doi: 10.1088/0264-9381/28/23/235017.
- [126] Ekrem Aydiner, Erdem Sucu, and İzzet Sakalli. Regular magnetically charged black holes from nonlinear electrodynamics: Thermodynamics, light deflection, and orbital dynamics. *Physics of the Dark Universe*, page 102164, 2025.
- [127] M. Chabab, H. El Moumni, S. Iraoui, and K. Masmar. Joule-thomson expansion of rn-ads black holes in $f(r)$ gravity. *Eur. Phys. J. C*, 78:632, 2018. doi: 10.1140/epjc/s10052-018-6134-0.
- [128] C. Lan, Y. G. Miao, and Y. X. Wang. Joule-thomson expansion of charged gauss-bonnet black holes in ads space. *Phys. Rev. D*, 98:084014, 2018. doi: 10.1103/PhysRevD.98.084014.
- [129] S. H. Hendi, B. Eslam Panah, M. Panahiyan, and M. S. Talezadeh. Geometrical thermodynamics and p - v criticality of black holes with power-law maxwell field. *Eur. Phys. J. C*, 77:133, 2017. doi: 10.1140/epjc/s10052-017-4693-0.
- [130] S. W. Wei and Y. X. Liu. Insight into the microscopic structure of an ads black hole from a thermodynamical phase transition. *Phys. Rev. Lett.*, 115:111302, 2015. doi: 10.1103/PhysRevLett.115.111302.
- [131] S. Nojiri, S. D. Odintsov, and T. Paul. Barrow entropic dark energy: A member of generalized holographic dark energy family. *Phys. Lett. B*, 825:136844, 2022. doi: 10.1016/j.physletb.2021.136844.
- [132] A. Sheykhi. Barrow entropy corrections to friedmann equations. *Phys. Rev. D*, 103:123503, 2021. doi: 10.1103/PhysRevD.103.123503.

- [133] S. Basilakos, A. Lymperis, M. Petronikoulou, and E. N. Saridakis. Barrow entropy constraints from black hole evaporation. *Eur. Phys. J. C*, 83:576, 2023. doi: 10.1140/epjc/s10052-023-11739-w.
- [134] N. Altamirano, D. Kubiznak, R. B. Mann, and Z. Sherkatghanad. Thermodynamics of rotating black holes and black rings: Phase transitions and thermodynamic volume. *Galaxies*, 2:89–159, 2014. doi: 10.3390/galaxies2010089.
- [135] S. R. Dolan and D. Dempsey. Bound states of the dirac equation on kerr spacetime. *Class. Quantum Grav.*, 32:184001, 2015. doi: 10.1088/0264-9381/32/18/184001.
- [136] D. R. Brill and J. A. Wheeler. Interaction of neutrinos and gravitational fields. *Rev. Mod. Phys.*, 29:465–479, 1957. doi: 10.1103/RevModPhys.29.465.
- [137] S. A. Teukolsky. Perturbations of a rotating black hole. i. fundamental equations for gravitational, electromagnetic, and neutrino-field perturbations. *Astrophys. J.*, 185:635–647, 1973. doi: 10.1086/152444.
- [138] E. Newman and R. Penrose. An approach to gravitational radiation by a method of spin coefficients. *J. Math. Phys.*, 3:566–578, 1962. doi: 10.1063/1.1724257.
- [139] S. Chandrasekhar. The solution of dirac’s equation in kerr geometry. *Proc. R. Soc. Lond. A*, 349:571–575, 1976. doi: 10.1098/rspa.1976.0090.
- [140] G. F. Torres del Castillo. Spin- $\frac{1}{2}$ perturbations of algebraically special solutions of the einstein-maxwell equations. *J. Math. Phys.*, 29:2078–2083, 1988. doi: 10.1063/1.527865.
- [141] A. Anderson and R. H. Price. Intertwining of the equations of black-hole perturbations. *Phys. Rev. D*, 43:3147–3154, 1991. doi: 10.1103/PhysRevD.43.3147.
- [142] J. Grain and A. Barrau. A wkb approach to scalar fields dynamics in curved space-time. *Nucl. Phys. B*, 742:253–274, 2006. doi: 10.1016/j.nuclphysb.2006.02.036.
- [143] D. N. Page. Particle emission rates from a black hole. iii. charged leptons from a nonrotating hole. *Phys. Rev. D*, 16:2402–2411, 1977. doi: 10.1103/PhysRevD.16.2402.
- [144] E. Witten. Dynamical breaking of supersymmetry. *Nucl. Phys. B*, 188:513–554, 1981. doi: 10.1016/0550-3213(81)90006-7.
- [145] R. Bluhm and V. A. Kostelecky. Spontaneous lorentz violation, nambu-goldstone modes, and gravity. *Phys. Rev. D*, 71:065008, 2005. doi: 10.1103/PhysRevD.71.065008.
- [146] B. F. Whiting. Mode stability of the kerr black hole. *J. Math. Phys.*, 30:1301–1305, 1989. doi: 10.1063/1.528308.
- [147] S. Chandrasekhar and S. Detweiler. The quasinormal modes of the schwarzschild black hole. *Proc. R. Soc. Lond. A*, 344:441–452, 1975. doi: 10.1098/rspa.1975.0112.
- [148] V. Cardoso and J. P. S. Lemos. Scalar, electromagnetic and weyl perturbations of btz black holes: Quasinormal modes. *Phys. Rev. D*, 63:124015, 2001. doi: 10.1103/PhysRevD.63.124015.
- [149] R. A. Konoplya and A. Zhidenko. Stability of higher dimensional reissner-nordström-anti-de sitter black holes. *Phys. Rev. D*, 78:104017, 2008. doi: 10.1103/PhysRevD.78.104017.
- [150] K. Akiyama et al. First m87 event horizon telescope results. vi. the shadow and mass of the central black hole. *Astrophys. J. Lett.*, 875:L6, 2019. doi: 10.3847/2041-8213/ab1141.
- [151] K. Akiyama et al. First sagittarius a* event horizon telescope results. vi. testing the black hole metric. *Astrophys. J. Lett.*, 930:L17, 2022. doi: 10.3847/2041-8213/ac6756.
- [152] Anamika Kotal, Ujjal Debnath, and Anirudh Pradhan. Cosmological parameter analysis and correspondence of f(R), f(G), f(T) gravity models within the (m, n)-type Barrow holographic dark energy framework. *Phys. Scripta*, 100(11):115302, 2025. doi: 10.1088/1402-4896/ae1a1b.